

REVIEW

[View Article Online](#)
[View Journal](#) | [View Issue](#)

Cite this: *J. Mater. Chem. C*, 2021,
9, 16110

Received 27th May 2021,
Accepted 13th August 2021

DOI: 10.1039/d1tc02441h

rsc.li/materials-c

Lanthanide-doped nanoparticles in photovoltaics –
more than just upconversion

Pinzheng Zhang,^{abc} Liangliang Liang^b and Xiaogang Liu^{id} *^{abc}

Development of photon conversion nanomaterials could principally leverage unutilized portions of the solar spectrum to address the increasing demand for renewable energy. However, improving photovoltaic performance using lanthanide-doped, spectral-converting nanomaterials remains a challenge. For photon upconversion, the most significant issues lie in their low quantum efficiencies and the need for high-power laser excitation. Despite these constraints, lanthanide-doped upconversion nanomaterials hold great promise to enhance the light-harvesting capacity and the conversion efficiency of existing solar cell modules. In this review, we highlight recent advances in developing high-efficiency upconversion nanoparticles for photovoltaic application. Special attention will be paid to fundamental energy transfer mechanisms, the survey of strategies for nanoparticle synthesis and surface modification, and various schemes of nanoparticle integration into photovoltaic devices. We also discuss future research directions and practical challenges in coupling upconversion nanomaterials with existing photovoltaic technologies.

1. Introduction

Harvesting underutilized portions of the solar spectrum for energy conversion has been the Holy Grail of Photovoltaics seeking to break the Shockley–Queisser limit.¹ Surpassing intrinsic limits meant that proposed solutions must bypass the model's defined assumptions. Upconversion and downconversion remain the most popular approaches to potentially harvest more visible-wavelength

photons under the same physical conditions *via* spectral conversion of underutilized portions in the solar spectrum.² In an upconversion process that involves the conversion of sub-bandgap near-infrared light into visible light for reabsorption by photovoltaic cells, the ceiling for improvement remains high with a conversion efficiency as high as 47.6% (AM 1.5G).³ Indeed, the earliest experimental studies by Trupke *et al.* on crystalline silicon (C–Si) photovoltaics with NaYF₄:Er³⁺ phosphors recorded a performance enhancement of 2.5%, a statistic that is sufficiently encouraging to pursue higher performances.⁴

However, a salient but much less discussed caveat behind this achievement is that such statistics were derived from concentrated photonic environments such as laser excitation. Thus,

^a Integrative Sciences and Engineering Programme, NUS Graduate School, National University of Singapore, 117456, Singapore. E-mail: chmlx@nus.edu.sg

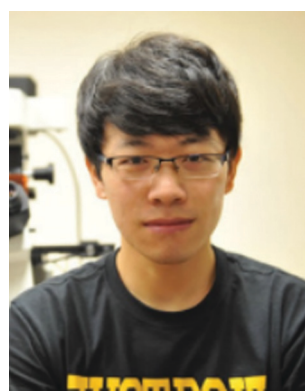
^b Department of Chemistry, Faculty of Science, National University of Singapore, 3 Science Drive 3, 117543, Singapore

^c The No. 1 Institute for Health, National University of Singapore, 117456, Singapore



Pinzheng Zhang

Pinzheng Zhang graduated from the National University of Singapore with a BEng in Materials Science and Engineering in 2019. He is currently pursuing his PhD in NUS Graduate School of Integrative Sciences and Engineering under the supervision of Professor Xiaogang Liu. His current research interest lies in the rational design of lanthanide–luminophore hybrids for upconversion and downconversion processes.



Liangliang Liang

Liangliang Liang obtained his BS degree in Materials Science from Nankai University. He received his MS degree in Condensed Matter Physics from Wuhan University and completed his PhD in the group of Professor Xiaogang Liu at the National University of Singapore. He is currently carrying out post-doctoral research work at the National University of Singapore. His research interests focus on optical super-resolution imaging and functional luminescent nanomaterials.

one should expect significantly smaller increments under standardized global conditions (AM 1.5G) or alterations would be necessary to create a similar, concentrated photonic environment to emulate photovoltaic enhancement of the same magnitude. Actual figures from photovoltaic architectures coupled between C-Si solar cell modules and upconverting layers represent subtle enhancement, which raises questions about unrealistic expectations. Meanwhile, upconversion materials are beginning to be used in second- and third-generation solar cells to improve overall performance.⁵

Herein we strive to offer a concise review of recent developments regarding lanthanide-doped nanoparticles for photovoltaics, noting a gradual shift of their application from first-generation C-Si solar cells to third-generation dye-sensitized solar cells (DSSCs).^{6,7} We first introduce prevailing upconversion mechanisms and various materials that can be employed to enhance photovoltaic efficiency. To initiate the discussion, we address inherent challenges in using lanthanide-doped materials in C-Si solar cells, after which we explore other types of photovoltaic designs. Furthermore, an assessment on incorporation of upconversion materials into DSSCs and high-performance, less stable perovskite solar cells is provided, where their functions in photovoltaics are elucidated. Moreover, we assess prospects of upconversion in solar cells, with a glimpse of the field's directions in coming years. Despite the less-than-ideal nature of upconversion in conventional C-Si photovoltaics, lanthanide-doped nanoparticles will remain to be versatile materials that serve well as valuable enablers of emerging photovoltaic technologies and applications.

2. Upconversion luminescence mechanisms

Upconversion (UC) is a nonlinear photonic process that typically involves absorption of two or more lower-energy photons, excitation energy accumulation, and energy transfer, followed

by emission of a single, higher-energy photon. This anti-Stokes photonic phenomenon dates to the 1960s, where it was first observed by the collective studies from Auzel, Feofilov, and Ovsyankin.⁸ UC is synonymous with lanthanides because of unique optical properties derived from 4f electrons and the concomitant 4f–4f interactions that make these elements highly attractive for basic research and potential applications. However, UC has since expanded to include molecules and dyes, with triplet states considered a viable alternative to lanthanides.⁹ Today, with research advances in this direction, UC mechanisms can now be broadly categorized into three classes: (i) lanthanide-based upconversion, (ii) dye-based upconversion, and (iii) hybrid upconversion (Fig. 1). A brief introduction to each of these classes is provided below.

2.1 Lanthanide-based upconversion

As mentioned earlier, lanthanides are much sought-after for UC studies due to their peculiar electronic properties. Comprising 14 elements in the 4f block of the periodic table from lanthanum (La) to lutetium (Lu), the lanthanide series feature the trivalent ionic state (Ln^{3+}) as their most stable oxidation state, containing a variety of energy levels from ultraviolet (UV) to the near-infrared (NIR) regions. Furthermore, lanthanide ions are characterized by sharp spectral features and electric-dipole forbidden intra-4f transitions with long excited-state lifetimes.¹⁰ As a result, their intermediate states can be utilized for energy accumulation within ladder-like energy levels, and energy can be transferred from one to another.

UC mechanisms between lanthanide ions can be broadly categorized into five types (Fig. 1), namely excited-state absorption (ESA), energy transfer upconversion (ETU), cooperative sensitization upconversion (CSU), photon avalanche (PA) and energy migration upconversion (EMU). ESA occurs when there exists an equal separation between the G and E1 as well as the E₁ and E₂ energy levels (Fig. 1a). Upon excitation of a lanthanide ion with a photon to metastable E1, it is possible to further excite it to E₂ with a second photon, a mechanism that bears some similarity to two-photon excitation.¹¹ Lanthanide ions that best demonstrate this mechanism are erbium (Er^{3+}), holmium (Ho^{3+}), thulium (Tm^{3+}) and neodymium (Nd^{3+}), which possess ladder-like energy arrangements that can be readily excited with diode lasers.⁸

Despite being governed by a similar two-photon process, ETU differs from ESA in that UC is achieved by excitation through energy transfer between a pair of adjacent ions. ETU is governed by populating a metastable level E1 from its ground state G on either of the two ions (Fig. 1b). This is followed by nonradiative dipole–dipole energy transfer that drives one ion to a higher energy state and the other ion to its ground state. The ultimate UC efficiency is reliant on the separation distance between the ion pair, which depends on parameters such as the concentration of the constituent lanthanide ions and their ratios. The most widely used UC ion pairs are Yb^{3+} coupled with either Er^{3+} , Ho^{3+} , or Tm^{3+} , primarily due to the advantages of Yb^{3+} as the sensitizer.¹² Yb^{3+} possesses a larger absorption cross-section at 980 nm ($^2\text{F}_{7/2} \rightarrow ^2\text{F}_{5/2}$) than other lanthanide ions,^{13,14} making ETU more favorable and less susceptible to concentration quenching. ETU can also occur in Er–Er pairs,^{15,16}



Xiaogang Liu

Xiaogang Liu received his BE degree in chemical engineering from Beijing Technology and Business University, China. He received his MS degree in chemistry from East Carolina University and completed his PhD at the Northwestern University. He then carried out postdoctoral work at the Massachusetts Institute of Technology for two years before joining the National University of Singapore in 2006. Currently, he sits as an associate editor for Nanoscale and serves on the

editorial boards of Research, Nanoscale Horizons, Chemistry – An Asian Journal, Advanced Optical Materials, Analysis and Sensing, Journal of Luminescence, and Journal of Physical Chemistry Letters. His research encompasses areas including nanostructured catalysis, optical nanomaterials, optogenetic neuromodulation, and X-ray imaging.

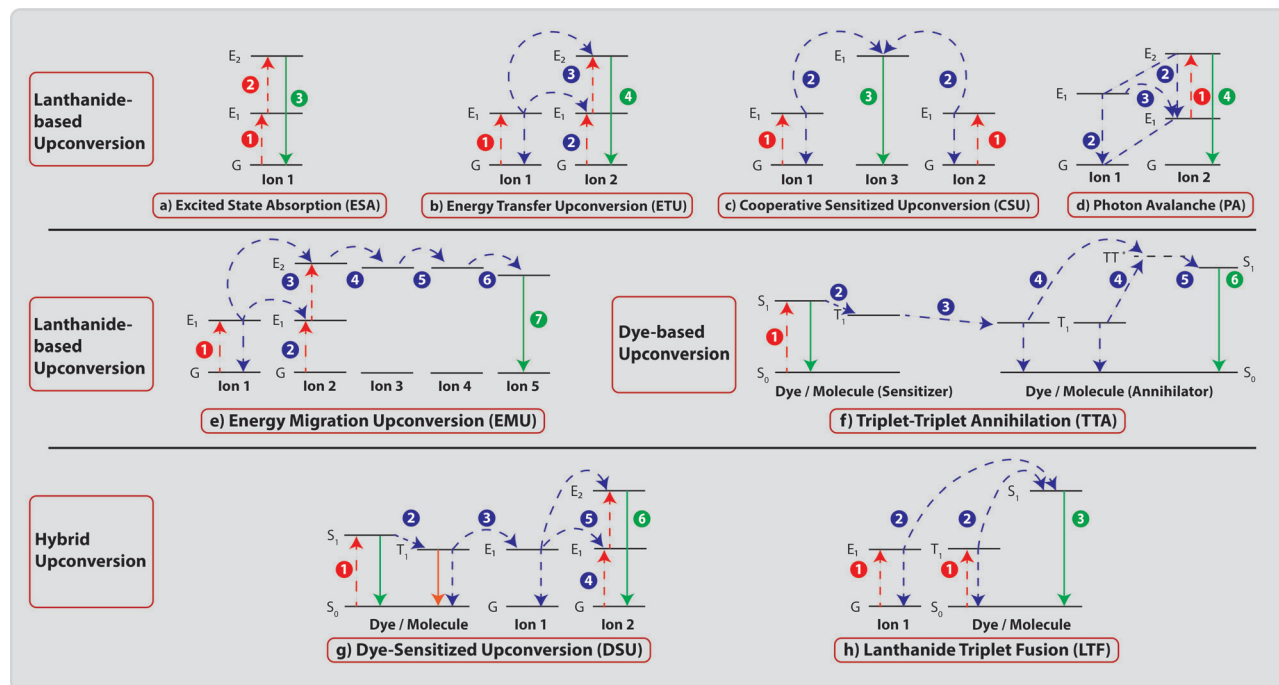


Fig. 1 Overview of principal upconversion processes in lanthanide-doped upconversion nanomaterials and dyes, which can be classified into three classes: lanthanide-based upconversion (a–e), dye-based upconversion (f), and hybrid upconversion (g and h). Lanthanide-based upconversion mechanisms encompass (a) excited state absorption (ESA), (b) energy transfer upconversion, (c) cooperative sensitization upconversion, (d) photon avalanche and (e) energy migration upconversion. Dye-based upconversion is characterized by (f) triplet–triplet annihilation (TTA). Lastly, a hybrid lanthanide-dye upconversion is possible with two possible pathways: (g) dye-sensitized upconversion (DSU) and (h) lanthanide triplet fusion (LTF). In each upconversion process, numbers 1–7 refer to various optical steps involved in photon upconversion. The red, blue and green/orange arrows represent the excitation, non-radiative transfers and emission processes, respectively.

particularly under 1523 nm excitation, an optimal spectral region for UC photovoltaics (Fig. 2). Notably, ETU is the most probable and efficient UC mechanism.¹⁷

The third possible UC mechanism is cooperative sensitization upconversion (CSU), which involves a pair of sensitizers and a third activator ion (Fig. 1c). This process begins with

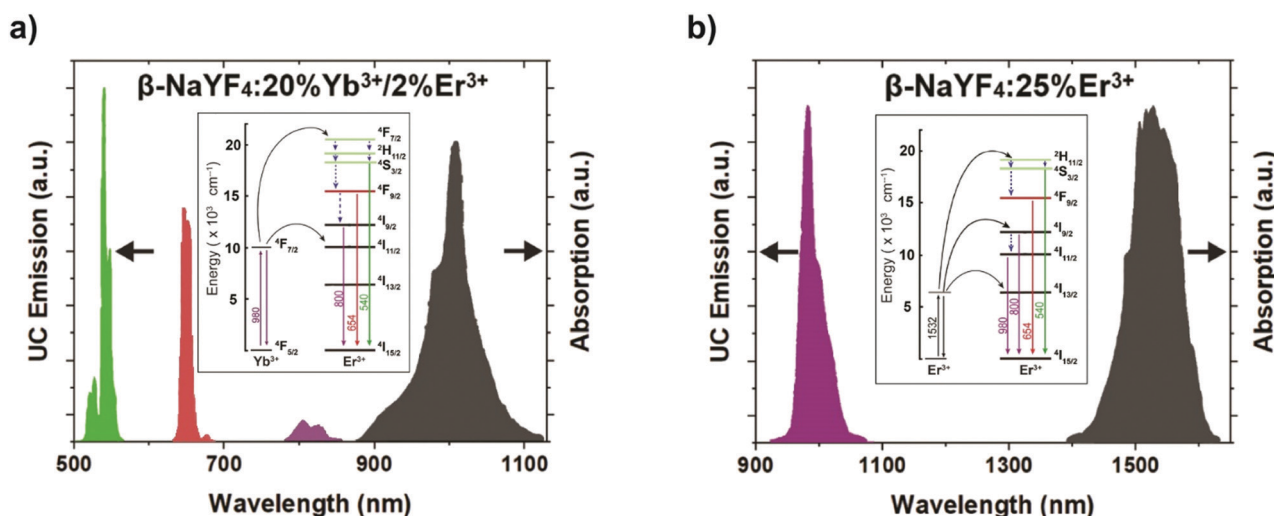


Fig. 2 Upconversion schemes from two most common lanthanide-based upconversion materials that are utilized in the field of photovoltaics. (a) Absorption and emission spectra of a Yb–Er ion pair system in a β - NaYF_4 host matrix. Inset: Energy level diagram illustrating energy transfer upconversion (ETU) involving Yb as the sensitizer under excitation at 980 nm, followed by sequential transfer to Er. (b) Absorption and emission spectra of an Er singly doped system in the β - NaYF_4 matrix. As a three-photon process is much less likely to occur than a two-photon upconversion, the intensity of the visible emission (not shown) is much weaker than its NIR counterpart. Inset: ETU involving a singly doped Er system in which Er functions as both the sensitizer and the activator under 1532 nm excitation. For energy diagrams shown above, solid lines denote excitation, energy transfer and radiative transitions, while dotted lines represent non-radiative transitions due to phonon relaxation in the host lattice.

simultaneous excitation of the sensitizer ions to their excited states, followed by cooperative transfer to the activator ion. This results in a higher excited state in which an upconverted photon is emitted. Compared to ESA and ETU, CSU is much less efficient because of the lack of a real intermediate energy level in the activator. CSU requires quasi-virtual pair levels for optical transitions as seen in Yb^{3+} – Tb^{3+} ion-pairing systems and consequently its high-power excitation is incompatible with photovoltaic application.^{10,18–20}

Meanwhile, photon avalanche (PA) involves an iterative ESA and a cross-relaxation loop between two interactive ions (Fig. 1d). To date, the best-known example is Tm-doped nanomaterials.²¹ While the looping process seemed attractive for harvesting large amounts of upconverted light, PA requires a certain excitation threshold and has a stipulated time delay.²² Hence, PA currently has limited value in UC applications and is considered incompatible with photovoltaic use.²³

Another interesting UC mechanism is energy migration upconversion (EMU), where it requires an intricate lanthanide combination of 4 components; (1) sensitizer, (2) accumulator, (3) migrator and (4) activator to facilitate long-range energy transfer (Fig. 1e). Additionally, to obviate the inimical cross-relaxation between the lanthanide ions, a core-shell structure is necessary to spatially isolate the sensitizer/accumulator and the activator, while the migrator ion is present at both layers to serve as an energy transfer bridge at the core-shell interface.²⁴ Initial research efforts to leverage this mechanism were primarily studied in a combinatory lanthanide system of Yb – Tm – Gd – X ($\text{X} = \text{Tb}, \text{Eu}, \text{Dy}, \text{or Sm}$),²⁵ with the focus of Gd embedded in the sublattice serving as a stable, high-energy migratory ion. This system is robust and widely used because NaGdF_4 host facilitates minimal energy losses during the migration process and the ability to generate a multitude of colors by switching the activating lanthanide.

Lately, a series of studies were performed to improve and expand the initial design, as well as achieving spatial optimization of lanthanide dopants without compromising UC emission.²⁶ A major advance in EMU is the design of migratory interlayers to segregate sensitizers and activators, preventing cross-relaxation quenching *via* interfacial energy transfer.^{27,28} In addition, this ensures the sensitizing core in UCNPs is sufficiently isolated from surface quenching. Thus far, Gd , Tb and Yb ions have demonstrated to be effective migratory entities that cater energy transfer in high ($\sim 32\,000\text{ cm}^{-1}$, $^6\text{P}_{7/2} \rightarrow ^8\text{S}_{7/2}$), medium ($\sim 18\,350\text{ cm}^{-1}$, $^5\text{D}_4 \rightarrow ^7\text{F}_5$) and low ($\sim 10\,000\text{ cm}^{-1}$, $^4\text{F}_{5/2} \rightarrow ^4\text{F}_{7/2}$) energy collisions,^{29,30} respectively.³¹ Such interlayers have great utility for harnessing the UC emission of NaErF_4 cores to produce intense red emission under 1532 nm excitation.³² To accomplish this, Zhou *et al.*³³ used a Yb -based sublattice at the interlayer to serve as an EMU channel to harness Er^{3+} emission. The harvested UC output can further activate other lanthanide dopants, generating emission with large anti-Stokes shifts. According to Blasse,³⁴ while Er^{3+} and other lanthanides can also serve as migratory entities, their UC effectiveness is more susceptible to surface quenching, which leaves room for further optimization and design.³⁵

2.2 Dye-based upconversion

Triplet-triplet annihilation (TTA) is the second class of UC mechanism that has attracted substantial attention due to its high internal quantum yield (Fig. 1f).^{36–40} In TTA, both the sensitizer and the annihilator are composed of chromophores in which UC occurs between the long-lived triplet states to generate radiative singlet-photon emission. TTA typically begins with excitation of the sensitizer from its ground to a singlet excited state ($\text{S}_0 \rightarrow \text{S}_1$), followed by intersystem crossing (ISC) to attain a triplet state ($\text{S}_1 \rightarrow \text{T}_1$). Generated triplet states in the sensitizer are then transferred to the triplet state in the annihilator *via* triplet-triplet energy transfer (TTET). Finally, the annihilator's triplet states are recombined to form excited singlet states, which then relax back to the ground state *via* a radiative transition.

In TTA, the processes that determine resultant emission wavelengths and UC efficiency lie on the relative energy level of the singlet and triplet states of both the sensitizer and the annihilator in the Jablonski diagram.⁴¹ Effective TTET typically requires the triplet energy of the sensitizer to be higher than that of the annihilator, even though there are several reported exceptions.^{42,43} Since this review focuses on the role of UC in lanthanide-doped photovoltaic nanomaterials, we limit our discussion of TTA to its mechanism and basic understanding as a parallel pursuit of upconversion in trivalent lanthanides. Comprehensive reviews by Li *et al.*^{13,44} and Kasper *et al.*^{13,44} are available. As an interesting development, lanthanide-coordinated complexes have been employed as NIR sensitizers for TTA with large anti-Stokes shifts ($\sim 0.95\text{ eV}$).⁴⁵ This approach presents a new direction for developing TTA-based UC with an expanded spectral range in the future.

2.3 Hybrid upconversion

While lanthanides and dye molecules were initially deemed incompatible in UC, recent work has revealed a cooperative relationship in which novel mechanisms have been discovered. To date, two mechanisms can be classified under the third class of lanthanide-dye hybrid upconversion: dye-sensitized upconversion (DSU) and lanthanide triplet fusion (LTF) (Fig. 1g and h). Both exploit the long-lived nature of abundant triplet states in organic molecules to interact with 4f electronic states in trivalent lanthanide ions.

Organic molecules are often coupled to lanthanide-doped upconversion nanoparticles (UCNPs) with excessively doped sensitizers to increase the absorption cross-section of lanthanide ions and broaden their spectral response. In addition, dyes can help mitigate deleterious concentration quenching with partial surface defect passivation and highly efficient energy transfer.^{46–49} Analogous to a molecular optical antenna, lanthanide emission can be augmented by a few orders of magnitude,^{50–52} making proposed applications feasible. However, most cases assumed that energy transfer between the molecule or dye and the lanthanide ion occurs from the singlet state of the molecular sensitizer, which is valid if the Förster resonance energy transfer (FRET) rate is faster than the ISC to the triplet ($\text{S}_1 \rightarrow \text{T}_1$).⁵³ In cases where ISC is more efficient than the singlet state FRET process, a Dexter-type energy

transfer from its triplet states can be realized if the lanthanide and triplet state energies are compatible.

DSU was employed by Schuck *et al.*⁵⁴ to explain lanthanide-dye interactions and the underlying properties of spin-triplet states in the dye antenna critical for UCNP sensitization. In their work with a conventional UCNP-dye system of NaYF₄:Yb/Er/Gd-IR806, variations in the composition of lanthanide content, specifically Gd, could modulate ISC rates and determine triplet populations. Heavily populated triplet states in the dye were then transferred to the Yb-Er activator pair, generating bright, upconverted luminescence through Dexter-type energy transfer. A recent finding corroborated the mechanism of triplet energy transfer; the proximity of UCNP to dyes could be used to control triplet dynamics.⁵⁵ Such control was attributed to the intense spin of unpaired 4f electrons in certain lanthanides.⁵⁶ The strong coupling between the organic molecule and the lanthanide was evident in Gd with the highest spin number, enabling highly efficient triplet generation and transfer.

Furthermore, LTF offers a simplified energy pathway with minimized energy losses and no reabsorption of upconverted light compared with conventional dye- or quantum dot-sensitized TTA-UC systems. LTF draws some resemblance to a dye-based upconversion mechanism through direct excitation of triplets as demonstrated by Kimizuka *et al.*⁵⁷ However, LTF is based on coupling effects in the UCNP-dye aggregate while the dye-based system is based on heavy-atom-induced spin-orbit coupling of the sensitizer alone. This lanthanide-dye hybrid mechanism underscores the potential synergistic interaction between the two and in fitting instances, how the properties of UC nanomaterials serve a secondary function to aid upconversion.⁵⁸ However, a successful LTF requires a suitable dye with compatible S₁ and T₁ energy levels and a lanthanide ion with complementary electronic transitions.

3. Lanthanide-doped materials in C-Si solar cells – a brief assessment

Crystalline silicon (C-Si) is the champion photovoltaic (PV) material with reported efficiencies as high as 26.7%, and it also dominates the commercial PV landscape with a 95% market share.⁵⁹ C-Si solar cells operate with a wavelength cut-off at 1110 nm ($E_g = 1.12$ eV); hence, lanthanide-doped materials as upconverting layers are expected to absorb wavelengths in the NIR-II and NIR-III ranges, which comprise up to 36.3% of the sub-bandgap photons.⁶⁰ In this section, we highlight UC material developments for C-Si photovoltaics and the underlying problem of incorporating UC materials into solar cells.

3.1 Benchmarking efficiencies of upconversion materials

While the 4f electrons of trivalent lanthanides are chemically inert, they are susceptible to phonon energies in the local environment. Hence, lanthanides are often doped into host materials with low phonon energies. Other desirable properties include high coordination numbers (CN \geq 6) and comparable ionic radii with an affinity for hard, oxophilic species.⁴⁷ The hexagonal phase (β) of NaYF₄ is the host matrix of choice.^{61,62}

It has been used in many UC applications since it facilitates highly efficient UC. For potential use in photovoltaics, knowledge of the absolute (external) quantum yield (QY) is important. The earliest quantitative measurement was made by van Veggel and Boyer, who determined that the quantum yield of β -NaYF₄: 20%Yb/2%Er microcrystal phosphors is \sim 3% at 20 W cm⁻², while nanoparticles reported a yield less than 1% under 976 nm excitation at 150 W cm⁻².⁶³ For use in C-Si PVs, the most studied material is β -NaYF₄: 25%Er micron-sized phosphors that boast a quantum yield of 5.1% under an irradiance of 0.188 W cm⁻² at 1523 nm.⁶⁴ Theoretically, while Ho³⁺ could be considered for incorporation into the NaYF₄ host for absorption in the 1150 to 1200 nm region (⁵I₈ \rightarrow ⁵I₆), its weak transition and the lack of an efficient energy transfer mechanism for UC have imposed severe limitations.⁶⁵⁻⁶⁷

Apart from NaYF₄: 25%Er, another material candidate for UC is Gd₂O₃:10%Er.^{68,69} While this material displays higher phonon energy ($\omega = \sim$ 440 cm⁻¹) than β -NaYF₄ ($\omega = \sim$ 350 cm⁻¹), on certain benchmarks, it displayed better performance than β -NaYF₄.^{68,70} Most notably, Meijerink *et al.*⁷¹ directly compared the two microcrystalline materials and concluded that Gd₂O₃ (QY = \sim 6.5%) is superior to β -NaYF₄ (QY = \sim 5.5%) at high-intensity excitation at 1510 nm. Another investigation by the same team concluded that the two materials are complementary in terms of performance and purpose; a β -NaYF₄ host lattice is better suited to broadband excitation, whereas Gd₂O₃ is appropriate for narrow spectral ranges under lower excitation power.⁷²

One reason for β -NaYF₄ to maintain superiority as an upconverting phosphor is its structural and size tunability.⁷³ The primary cause of low quantum yields recorded with colloidal phosphors is surface quenching since most lanthanide ions are exposed to the surrounding environment, which creates more nonradiative pathways.⁷⁴⁻⁷⁶ Nanophosphors are also susceptible to high numbers of surface defects, which quench their luminescence further.^{77,78}

The design of core-shell structures has proven highly reliable to increase the overall QY of colloidal phosphors, to which β -NaYF₄ has contributed the most.⁷⁹⁻⁸² For instance, an inert shell on β -NaLnF₄ (Ln = Lu, Gd, or Y) can suppress most surface quenching effects.⁸³⁻⁸⁵ Precise shell growth up to 10 nm has several advantages: (i) improving the overall quantum yields of the nanophosphors (QY = \sim 3%) and bridging the gap to their bulk counterparts, (ii) operating at a lower irradiance, and (iii) accommodating a higher concentration of lanthanide dopants, which increases the QY.^{79,80,83-86} β -NaYF₄ has proven more beneficial than other nanoscale lanthanide-doped phosphor materials such as Eu/Tb/Ce-doped La/CePO₄,⁸⁷⁻⁸⁹ which face synthetic challenges to create similar core-shell structures. Furthermore, to our knowledge, no equivalent core-shell strategy for Gd₂O₃ nanocrystals has been formulated.

While UC phosphors can exhibit appreciable UC efficiencies, these are only achievable under high excitation irradiances, and it is desirable to reduce excitation power density as much as possible. In field-testing under illumination of AM1.5G 1-sun, the corresponding power density is much lower at 0.1 W cm⁻² (or 1000 W m⁻²). The host materials for lanthanide doping are

generally insulators with large bandgaps. Hence, these phosphors have a shallow absorption cross-section for sensitization. Although there are solutions to address limitations for down-conversion (DC) and downshifting (DS), such as by doping transition metal ions and coupling with semiconductors or chromophores, the circumstances are more dire for UC, especially in the spectral range beyond 1100 nm.⁴⁷ At present, Ni^{2+} is the only transition metal ion suitable for broadband UC with absorption coverage between 1100 and 1350 nm.^{90,91}

Furthermore, UC is a nonlinear photonic process with the general relation of $I \propto P_{\text{exc}}^n$, there is a certain degree of power dependence to attain an adequate UC quantum yield.^{92,93} As such, its QY is intrinsically low under diffuse or low-power excitation. To put this into perspective, the recorded minimum power density under 1523 nm excitation to reach an absolute quantum yield of 3.9% for $\text{NaYF}_4\text{:Er@NaYF}_4$ core-shell nanocrystals is $\sim 18 \text{ W cm}^{-2}$, which is still two orders of magnitude higher than the overall AM 1.5G irradiation.⁹⁴ It is necessary to circumvent the restrictive AM 1.5G condition for PV, such as device and optical engineering (e.g., luminescent concentrators) to stimulate a laser-like excitation environment and replicate similar UC efficiency.

3.2 Limitations and challenges of upconversion materials in real-time solar cell testing

Bifacial C-Si PVs are often used with upconverters. For usable upconverted radiation to be received at the back end of the PV

module, a rear reflector is installed to redirect upconverted photons (Fig. 3a).⁹⁵ In general, for UC enhancement, $\text{NaYF}_4\text{:Er}$ microparticles are chosen over nanocrystal counterparts. Solar cell performance can be quantified by measuring the increments in two important metrics: the external quantum efficiency (EQE) and the short circuit current (J_{sc}).

The first field test, conducted by Trupke *et al.* in 2004, recorded 2.5% EQE under intense monochromatic excitation at 1523 nm.⁴ While it should be possible to raise the EQE to an upper limit of 14.0%, the challenge is to reduce irradiance without compromising the EQE.⁹⁶ This can be achieved in part by solving design-related issues such as solar cell reflection losses, raising lanthanide doping levels, and improving upconverter materials, as demonstrated by several groups over the years.^{97–99} The best-optimized upconverter solar cell device based on $\text{BaY}_2\text{F}_8\text{:30%Er}$ offers EQEs of 9.5% with significantly lower excitation of 0.47 W cm^{-2} at 1520 nm. However, this only translates to a modest improvement of the short circuit current by 0.55% (17.2 mA cm^{-2}) and it does not exclude the need for increased solar concentration by 94-fold.¹⁰⁰ A similar physical test was also conducted on $\text{NaYF}_4\text{:Er@NaLuF}_4$ nanocrystals with an upconverter device EQE of 1.18% (Fig. 3b),⁸⁵ implying that the short circuit current on C-Si PVs is likely to be even lower. This also suggests that although effective core-shell strategies have largely suppressed nonradiative pathways, the efficiency disparity is still apparent as properties of submicron

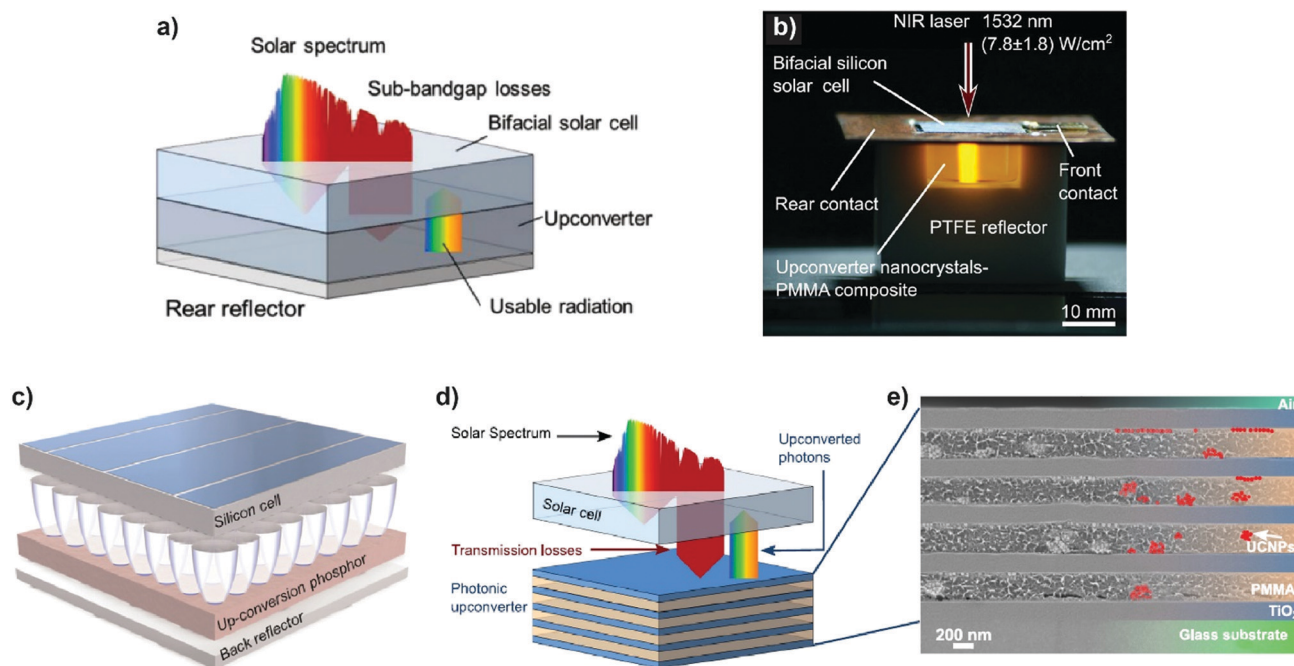


Fig. 3 (a) A simplified schematic diagram of a bifacial crystalline silicon photovoltaic (C-Si PV) is tested with an upconverter device. The upconverter device is placed on the rear of the solar cell alongside a reflector. (b) Image of the experimental setup of the UC integrated bifacial C-Si PV where the upconverter layer now consists of $\text{NaYF}_4\text{:25% Er}$ nanocrystals dispersed in a PMMA matrix. (c) Artistic impression of a UC-PV with a regular two-dimensional array of integrated CPC optics as concentrators positioned at the rear and adjacent to the bifacial solar cell. Gaps between the layers are only for illustrative purposes. (d) Schematic of the proposed Bragg structure, which functions as a photonic crystal to amplify the local density of states as a means of luminescence amplification. (e) Cross-section of layers constructing the photonic upconverter Bragg structure, which consists of alternating layers of UCNPs in PMMA and TiO_2 . (Reproduced with permission from ref. 60, 85, 102 and 103, copyright 2015 and 2021, Wiley-VCH Verlag GmbH & Co. KGaA, AIP Publishing, Elsevier and Nature Publishing Group).

crystals, such as light scattering and optical trapping, are secondary factors that result in generally higher UC quantum yields.¹⁰¹

Because the significantly lower absorption coefficient (45.1 cm^{-1} in BaY_2F_8 vs. 10^6 cm^{-1} in C-Si) is the leading cause of the less-than-ideal EQE, recent work has focused on optical engineering and solar concentration to enable UC converters to perform better under natural sunlight conditions.¹⁰⁰ The concept of high-concentration optics for enhanced UC efficiency was often used as a facile and direct method to generate intense excitation under diffuse, broadband solar illumination.¹⁰⁴ One specific approach is to integrate compound parabolic concentrators at the rear of bifacial solar cells to generate an intense excitation beam of sub-bandgap light while efficiently collecting the diffuse UC light (Fig. 3c). This helps to raise the EQE to 1.80% under a 7 sun equivalent of broadband NIR excitation.¹⁰² Another method to increase the UC output of phosphors is to modify the local density of states, in which both plasmonic and dielectric approaches are pursued.^{103,105} The most frequent strategy is a multi-layered Bragg structure, in which microcavities increase the overall yield (Fig. 3d and e).^{106,107} Presently, the external QY of Bragg-assisted UC $\beta\text{-NaYF}_4\text{:25%Er}$ nanocrystals can reach 16% with an enhancement factor of 480, and potentially it can be further increased with microcrystalline phosphors. However, even with such improvements, the overall performance contribution to C-Si PV remains $\sim 1\%$.

4. Lanthanide-doped nanoparticles in DSSCs

Dye-sensitized solar cells (DSSCs) are third-generation photovoltaic technologies in which power conversion efficiency has reached 11.9%.⁵⁹ Based on the conventional absorption threshold of 750 nm ($E_g = 1.65 \text{ eV}$), the fraction of harvestable sub-bandgap photons is 65% and equates to 46% of the power in the AM1.5G spectrum.⁶⁰ The shorter wavelength cut-off also implies that the selection of lanthanides for UC phosphors has expanded, as seen in Fig. 5a. For instance, $\beta\text{-NaYF}_4\text{:20%Yb/2%Er}$ nanophosphors that operate under 980 nm excitation for Yb sensitization can be used. C-Si PVs and DSSCs also differ in the complementary function of lanthanide-doped phosphors. Beyond upconversion and light scattering, they can also function as internal counter-electrodes and electronic additives to facilitate electrochemical processes between the photoanode and electrolyte.⁶

4.1 Lanthanide-doped nanomaterials as spectral converters

Based on the Shockley-Queisser model, the expected efficiency limit of DSSCs is 28.2%. The DSSC efficiency, typically less than 10%, suggests that slight improvements in the device may bridge the efficiency disparity.¹⁰⁸ Reducing the loss of potential from 0.75 to 0.4 eV can ideally produce a DSSC with 20% efficiency.¹⁰⁹ Compared to C-Si, the shorter wavelength cut-off in typical DSSCs means more lanthanide ions usable for upconversion. This is especially advantageous if the sensitizers (Yb and Nd) can be used in tandem to perform ETU (Fig. 4).¹¹⁰

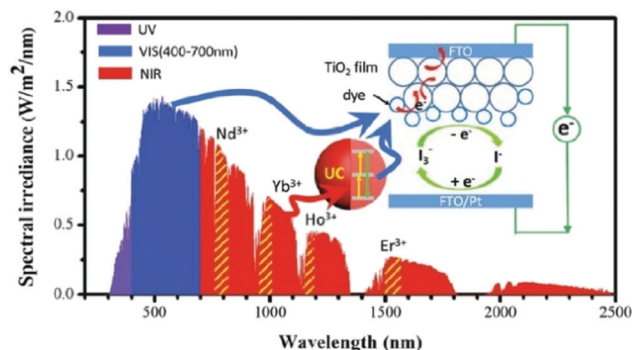


Fig. 4 Regions of spectral overlap with various lanthanides having luminescent transitions within the AM1.5G spectrum. In DSSCs, only the visible light is harvested for photovoltaic purposes. The NIR region can be covered by Nd ($\sim 808 \text{ nm}$), Yb ($\sim 980 \text{ nm}$), Ho ($\sim 1170 \text{ nm}$), and Er ($\sim 1520 \text{ nm}$). (Reproduced with permission from ref. 6, copyright 2018, Royal Society of Chemistry).

These two factors suggest that the role of spectral converters is more significant in closing the energy gap in DSSCs than in C-Si PVs.

While co-sensitization with multiple dyes is a sensible method to raise the efficiency limits of DSSCs by achieving a panchromatic spectral response, this approach faces challenges such as nonradiative cross-relaxation between sensitizers.^{116–119} Henceforth, luminescent spectral converters, which are externally attachable, can be an elegant solution for tandem solar coverage but with pure photonic coupling. External upconverting spectral converters are applied similarly to C-Si solar cells.

Unlike the case where the range of lanthanide-doped hosts used are limited to the several few in C-Si PVs, a wide range of hosts have been used for DSSCs, including fluorides, oxides and, oxyfluorides. Table 1 summarizes various lanthanide-doped hosts used as spectral converters, accompanied by recorded short circuit currents (J_{sc}) and efficiencies (η). When only pure photonic converters are applied, enhancements are small. For instance, Demopoulos *et al.*¹¹² demonstrated PV enhancements using a thick, dense UC layer and microcrystals for better light scattering to compensate for the low absorbance of lanthanide-doped materials. The direct UC contribution was determined as $\sim 1\%$ of the overall 10.2% enhancement when measured under AM1.5G conditions instead of monochromatic 980 nm laser excitation.

To further enhance UC contribution to external spectral converters, one of the possible ways is to improve the existing rear reflector region. As demonstrated by Ramasamy and Kim using triply doped $\beta\text{-NaGdF}_4\text{:Yb/Er/Fe}$ microcrystals as UC emitters, the UC output could be enhanced through surface plasmon amplification by coupling with a thin Ag microfilm.¹¹⁴ Large particles were proven as efficient light-reflectors for far-field light scattering due to their larger scattering cross-sections according to the Mie Theory.¹²⁰ This consideration was corroborated with a separate study by Lee *et al.*¹²¹ with similar architectures, although PV characterization was not provided and monochromatic laser pumping was used for optical excitation. Nevertheless, the multi-fold enhancement in absorption and the

Table 1 Summary of various UC phosphors used in the DSSC externally, accompanied with their synthesis method, optical properties and their figures of merit on the overall improvement (based on η metric) of photovoltaic device

Upconversion phosphors	Synthesis method	Emission (nm)	Sensitizer	J_{sc} (mA cm ⁻²)	η (%)	Enhancement (%)	Ref.
Y ₃ Al ₅ O ₁₂ :3%Yb/0.5%Er	Solid-state reaction	563	N719	—	—	—	111
β -NaYF ₄ :18%Yb/2%Er	Hydrothermal	510–570 640–680	N719	17.91	7.36	10.2	112
Yb ₂ O ₃	Commercial source	450–550 640–730	N719	16.12	9.21	—	113
β -NaGdF ₄ :18%Yb/2%Er/30%Fe (with Ag particles)	Coprecipitation	510–570 640–680	N719	12.62	7.04	21.3	114
β -NaYF ₄ :Yb/Er	Hydrothermal	510–570 640–680	C106	22.73	10.76	19.29	115

large increase in the optical path length were determined as the main contributions to enhanced PV performance.

Owing to the chemically inert nature of lanthanide-doped material hosts, UC phosphors have the advantage to be directly incorporated into DSSC devices to serve as internal spectral converters. This can be either by attachment to a mesoporous TiO₂ matrix at varying degrees (Fig. 5a–c) or in the electrolyte layer (Fig. 5d and e). The general role of UC phosphors in such a configuration is to achieve direct photonic coupling with dye molecules, enabling upconverted photons from phosphors to be passed to neighboring dye molecules. Table 2 summarizes various types of UC phosphors that have been incorporated into DSSCs.

The concept of using Yb/Er-codoped LaF₃ phosphors and their direct incorporation into TiO₂ as a nanocomposite was first conceived by Shan and Demopoulos.¹²² Their initial attempt proved ineffective as the multilayer structure resulted in a slight decrease in overall performance, perhaps because

the UC layer introduced surface recombination centers between the UCNP, the dye and the electrolyte. Moreover, the spectral mismatch between the dominant red emission of phosphors and the absorption of the N719 dye caused poor UC utilization. On the other hand, β -NaYF₄:20%Yb/2%Er UCNP were employed by Yuan *et al.*, who demonstrated that small nanoparticles (~20 nm) can penetrate the mesoporous scaffold of the TiO₂ photoanode and serve as nanoscale light scattering centers to further improve PV performance.¹²³ However, UCNP loading without morphological control inevitably creates more detrimental charge recombination centers, as reflected by the associated lower fill factor figures.¹²⁴

Contemporary UC phosphors for DSSCs often adopt a general core-shell structure that applies to both nanoparticle and micro-crystalline phosphors to mitigate surface quenching due to multiphonon relaxation or unwanted charge recombination. For nanoparticle phosphors, shell growth can involve either inert silica (SiO₂) or a crystalline NaYF₄, both of which can

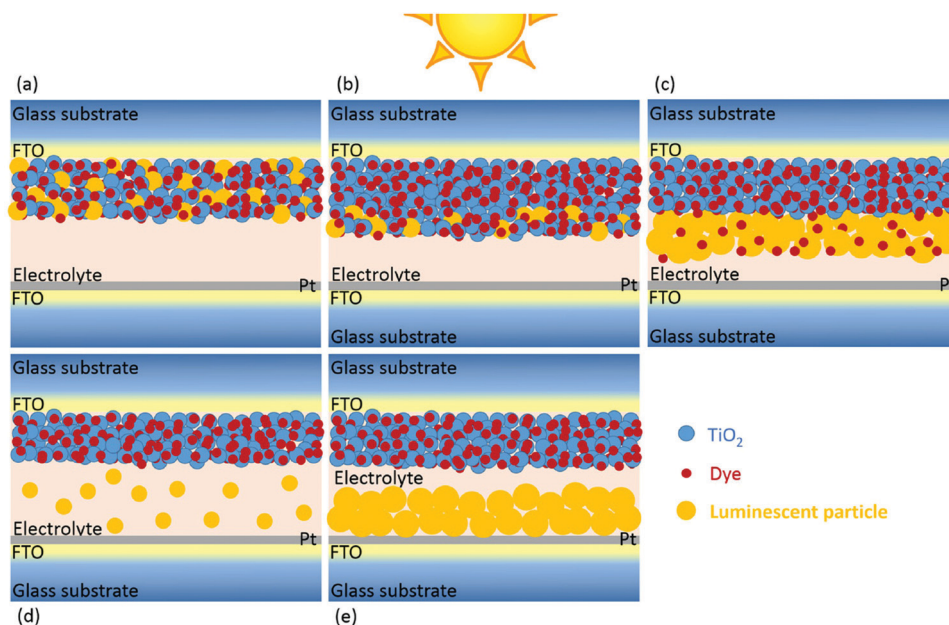


Fig. 5 Simplified schematics of modified DSSC cell architectures, in which upconverting lanthanide-doped nanomaterials are incorporated into the solar cell as internal spectral converters at multiple positions. It can be either (a and b) inside the mesoporous TiO₂ photoanode layer, (c) attached next to the TiO₂ layer, or (d and e) dispersed inside the electrolyte medium. The final placement of these UC phosphors in the DSSC ultimately depends on the method of synthesis for lanthanide introduction, the preparation of the TiO₂ photoanode paste, and the size of the UC phosphors. (Reproduced with permission from ref. 117, copyright 2017, Wiley-VCH Verlag GmbH & Co. KGaA).

Table 2 Summary of various UC phosphors used in DSSC internal structures, their synthesis methods, types of incorporation, upconversion optical properties and their contributions to the improvement (based on η metric) of photovoltaic devices

Upconversion phosphors	Configuration type	Synthesis method	Emission peaks (nm)	Sensitizing dye	J_{sc} (mA cm ⁻²)	η (%)	Enhancement (%)	Ref.
LaF ₃ :Yb/Er	c	Solvothermal	543, 655	N719	6.34	2.66	−1.13	122
β -NaYF ₄ :20%Yb/2% Er	a	Thermal decomposition	540, 660	Z907	12.5	2.8	3.73	124
β -NaLuF ₄ :20%Yb/2% Er	a	Coprecipitation	407, 520, 540, 654	N719	16.42	7.58	27.18	126
β -NaYF ₄ :18%Yb/2%Er@TiO ₂	c	Hydrothermal	525, 543, 655	N719	13.40	7.22	16.26	127
β -NaYF ₄ :20%Yb/2%Er@SiO ₂	a	Solvothermal	540, 660	N719	13.03	6.34	6.38	128
β -NaYF ₄ :18%Yb/2%Er@SiO ₂ @Au	c	Hydrothermal	525, 543, 655	N719	15.84	8.23	14.68	129
β -NaYF ₄ :20%Yb/2% Er@SiO ₂ @TiO ₂	c	Hydrothermal	500–560, 630–680	N719	19.97	9.21	18.08	125
β -NaYF ₄ :20%Yb/2%Er@ SiO ₂ @Au@TiO ₂	b	Hydrothermal	525, 541, 655	N719	18.62	7.79	28.10	130
β -NaYF ₄ :20%Yb/2%Er@NaYF ₄	a	Thermal decomposition	522, 540, 549, 656	N719, N749	18.3	9.15	5.54	131
β -NaYbF ₄ :2%Er@NaYF ₄ :30%Nd	a	Coprecipitation	406, 540, 650	N719	15.50	5.24	5.86	132
β -NaYF ₄ :20%Yb/2% Er@NaYF ₄ :Eu	b	Coprecipitation	408, 525, 540, 660	N719	12.89	7.15	6.36	133
Gd ₂ O ₃ :3%Yb/1%Ho	b	Precipitation	525–570, 635–675	N719	17.09	7.40	6.70	134
Y ₂ O ₃ :5%Yb/1%Ho	a	Complex precursor solution	545, 650, 779	N719	18.97	9.82	10.33	135
Y ₂ O ₃ :1%Yb/1%Er	b	Precipitation	510–570, 625–700	N719	13.68	6.68	12.40	136
Y ₂ O ₃ :3%Yb/0.2%Ho	c	Hydrothermal	550, 654, 788	N-3	21.90	7.59	30.00	137
Y ₂ CaZnO ₅ :5%Yb/0.5%Er	b	Sol-gel	535, 556, 668	N719	13.28	6.01	33.00	138
CeO ₂ :Yb/Er@SiO ₂ @Ag	c	Electrospinning	550, 660, 680	N719	16.24	8.17	22.86	139
YbF ₃ :Ho/TiO ₂	a	Hydrothermal	525, 540, 640, 660, 750	N719	18.58	8.00	23.00	140
β -NaYF ₄ :Er/Yb	d, e	Hydrothermal	510–570, 640–680	C106	18.00	9.48	5.10	115
β -LiYF ₄ :Er/Yb	c	Hydrothermal	522–556, 648–670	N719 + SPSQ2	22.16	10.53	N.A.	141

Note: The type of configuration is classified according to Fig. 6: **a** and **b**, inside the mesoporous TiO₂ photoanode layer; **c**, attached next to the TiO₂ layer; **d** and **e**, dispersed inside the electrolyte medium.

improve upconversion efficiency and decouple size-dependent scattering.^{128,131–133} However, the growth of a crystalline shell is preferred when a third-type lanthanide, in addition to the conventional Yb–Er pair, is added to prevent cross-relaxation, as seen in cases of Nd and Eu cooping.^{132,133} Another method to address the deleterious issues is to construct heterostructures with a nanoscale TiO₂ scaffold that facilitates interfacial photo-induced charge separation while suppressing charge recombination, as exemplified in YbF₃:Ho/TiO₂ hybrids.¹⁴⁰

Given the size incompatibility between sub-microcrystalline UC phosphors and the pore size of the TiO₂ scaffold, UC phosphors are often incorporated into DSSCs as a separate upconverting, light-scattering layer. To suppress charge recombination, microcrystals are coated with an external shell. A TiO₂ shell is an elegant solution because it also creates mesoporous sites to increase dye loading.^{125,127,130} For instance, Liang *et al.*¹²⁵ developed sub-micron bifunctional UC phosphors, with an inner SiO₂ shell as an electrical isolation layer and an outer TiO₂ shell for further dye loading (Fig. 6a). The functionalized DSSC was complemented by the 58.6% increase in dye loading, increasing DSSC performance to 9.21% (Fig. 6b). Furthermore, likened to strategies considered to enhance UC effects in C–Si PV devices, plasmonic components can be included in internal UC phosphor layers to amplify UC emissions from the phosphors.^{129,130} This empowerment can come from either one or a combination of the following mechanisms: far-field scattering, near-field coupling, hot electron transfer and plasmon resonant energy transfer.¹²⁰ Other than fluoride-based materials, lanthanide-doped oxide hosts can be used as UC phosphors due to

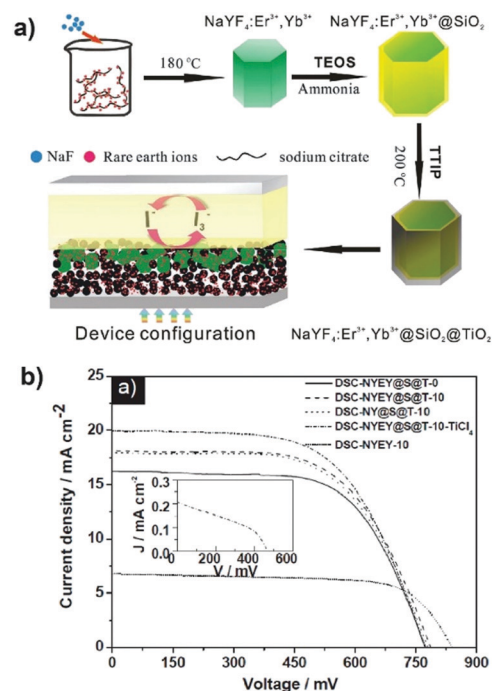


Fig. 6 (a) The overall experimental process to obtain β -NaYF₄:20%Yb/2%Er@SiO₂@TiO₂ micro-prisms and incorporation of the functionalized phosphor into a DSSC device. (b) J – V response of DSC-NYEF@S@T-10-TiCl₄ under illumination at 980 nm (inset) and J – V characteristics under one-sun illumination. Device properties are characterized over different phosphor composite loadings, lanthanide doping amounts, and post-treatment effects. (Reproduced with permission from ref. 125, copyright, 2013, Wiley-VCH Verlag GmbH & Co. KGaA.)

their high stability, despite comparatively high lattice phonon energies.^{134–139}

4.2 Lanthanide-doped nanomaterials as electronic additives

The anatase phase of TiO_2 is the photoanode material of choice for DSSCs, but several issues remain. Its mesoporous structure is laden with lattice defects after synthesis.¹⁵⁰ While certain shallow defects such as Ti^{3+} can act as essential n-type dopants for charge transport and conductivity improvement,¹⁵¹ there are also defects with deep traps, such as oxygen vacancies, which form recombination centers. These deep traps can lower the quasi-Fermi level of TiO_2 , decreasing conductivity and hindering charge transport. Henceforth, dopants are often used to create shallow defects in TiO_2 for improved electronic properties, while simultaneously passivating deep traps.¹⁵²

Besides their ability to broaden light absorption and instigate spectral conversion from NIR to visible light, trivalent lanthanides can act as p-type dopants to substitute Ti^{4+} ions in their lattice sites upon incorporation into a TiO_2 photoanode layer.¹⁵³ As the CB edge of anatase TiO_2 is occupied by 3d bands of Ti^{4+} ,¹⁵⁴ lanthanide substitution can manipulate the CB states for better alignment with dye sensitizers and electrolytes, thereby improving charge transport and raising Fermi levels. This was first demonstrated by Li *et al.*¹⁴² who found that Tm/Yb-codoped Lu_2O_3 nanopowder on the photoanode helped increase the Fermi level of TiO_2 . The overall increase by 11.11% in DSSC efficiency was a combined contribution of the increased photocurrent and open-circuit voltage through the p-type doping, and to a lesser extent due to upconversion luminescence from Tm centers, though they did not quantify the contributions of the two mechanisms. Similar work was undertaken by Xie *et al.*,¹⁴³ in which Tm and Yb lanthanide ions were directly incorporated into a TiO_2 matrix during photoanode synthesis together with trivalent lanthanide precursors. This method was also adopted later for doping other lanthanide ions, which resulted in significant DSSC efficiency improvements (Table 3).^{144–146} Lanthanide doping could also promote the formation of large and uniform TiO_2 nanoparticles for enhanced dye adsorption. Doping Ho/Er, Yb, and F ions into a TiO_2 matrix can be considered as p-type doping into the DSSC structure. The addition of F dopants not only enhances upconversion luminescence, but also improves the crystallinity of TiO_2 due to suppression of brookite and rutile phase formation.¹⁴⁹ This explains the greatly improved device conversion efficiency of 8.93% reported by Yu *et al.*¹⁴⁴

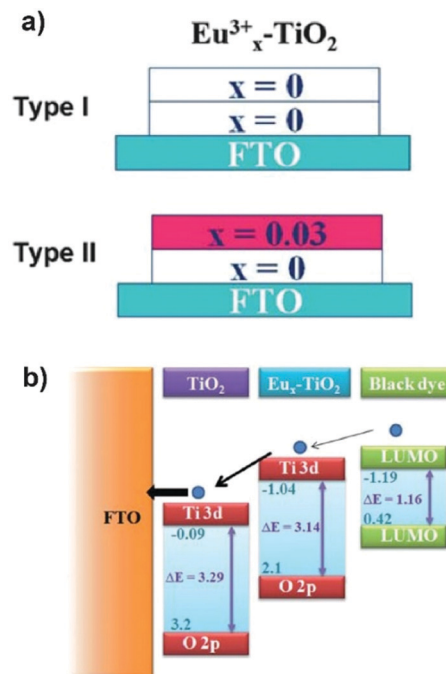


Fig. 7 (a) A simplified schematic of double layered TiO_2 photoanodes, where Type I is used as the control device, while Type II in the top TiO_2 layer with 3% Eu doping, functions as a secondary scattering layer in a DSSC test device. (b) Proposed energy level diagram of the type II structure. (Reproduced with permission from ref. 146, copyright 2010, Royal Society of Chemistry.).

While the effect of p-type doping from trivalent lanthanides was not fully understood, Liu *et al.*¹⁴⁶ postulated a mechanism to the increased photocurrent, shown in energy level diagrams (Fig. 7). In the double-layered photoanode (Fig. 7a), the lanthanide-doped layer serves as a mediating charge carrier due to the increased Fermi energy level that facilitates faster charge separation between photogenerated carriers. Therefore, charge recombination is less likely (Fig. 7b). It might be intuitive to increase lanthanide doping further to match the energy level of the sensitizing dye for more efficient charge separation, but additional aliovalent doping inevitably creates more interstitial defect centers, which can serve as charge traps for photoinduced electrons and holes. Therefore, alternative hosts such as lanthanide-doped YF_3 and YOF are considered for controllable, high-concentration doping.^{147,148}

Table 3 Various UC phosphors used in the DSSC photoanode layer as p-type dopants, their synthesis method, upconversion optical properties and overall improvement (based on η metric) of the photovoltaic device

Upconversion phosphors	Synthesis method	Emission peaks (nm)	Sensitizing Dye	J_{sc} (mA cm^{-2})	η (%)	Enhancement (%)	Ref.
$\text{Lu}_2\text{O}_3:0.4\%\text{Tm}/2\%\text{Yb}$	Coprecipitation	476, 653	N719	13.41	6.63	11.11	142
$\text{TiO}_2:\text{Tm}/\text{Yb}(3.33\%)$	Hydrothermal	475	N719	15.52	7.05	10.00	143
$\text{TiO}_2:\text{Ho}/\text{Yb}/\text{F}$	Hydrothermal	543, 644, 751	N719	21.60	8.93	40.85	144
$\text{TiO}_2:\text{Er}/\text{Yb}/\text{F}$	Hydrothermal	525, 545, 665, 800	N719	16.30	7.08	31.11	149
$\text{TiO}_2:\text{Er}$	Sol-gel	435, 535, 640–700	N719	13.38	6.63	62.90	145
$\text{TiO}_2:\text{Eu}$	Hydrothermal	—	N749	7.06	3.43	55.9	146
$\text{YF}_3:20\%\text{Yb}/2\%\text{Er}$	Thermal Decomposition	525, 545, 656	N719	15.58	7.90	35	147
$\text{YOF}:20\%\text{Yb}/2\%\text{Er}$	Hydrothermal	510–560, 640–690	N719	15.43	7.22	23.0	148

4.3 Lanthanide-doped nanomaterials in DSSC counter electrodes

On limited accounts, lanthanide-doped upconversion materials can potentially serve as replacement components in DSSCs. In a typical DSSC, Pt-coated fluorine-doped tin oxide (FTO) was used as a counter electrode to facilitate and catalyze the redox reaction of the I^{3-}/I^- electrolyte. While Pt is preferred for making highly efficient DSSCs due to its highly prized properties, such as high catalytic activity and stability, its material cost is an issue that needs to be addressed.¹⁵⁵ A common solution is to capitalize on advanced nanotechnologies that utilize less materials to deliver the same or a better performance. For instance, Pt nanoparticles are gradually adopted because of their high surface areas and higher-density catalytic sites.¹⁵⁶

The other approach is *via* the functional replacement of Pt, which is an ongoing research effort. Beyond economical and material considerations, an ideal counter electrode material should have the following properties: high transparency, resistance against corrosion under electrolyte cycling, high surface area for sufficient catalytic sites, and low electrical resistance to facilitate charge transfer. Given those technical requirements, composite fabrication based on common fluoride- and oxide-based lanthanide hosts is incompatible. This is evident from the work by Ambapuram *et al.*,¹⁵⁷ who developed a SnS composite counter electrode using sandwiched $\text{CeO}_2\text{:Yb/Er}$ upconversion particles, achieving a DSSC efficiency of 9.52%. However, their method requires a separate treatment step for the TiO_2 film and the incorporation of carbon into the counter electrode. Despite these modifications, the Pt-based counter electrode is still superior to SnS- or carbon-based constituents.

Lanthanide-doped conductive materials are alternative choices as DSSC counter electrodes. Thus far, progress has been sluggish, with only one study reported by Cao and co-workers.¹⁵⁸ They integrated Yb/Er-codoped upconverting FTO nanoparticles directly into a conductive material. Harvested NIR light between 750 and 1000 nm was upconverted to red light due to Yb–Er-mediated dye sensitization (Fig. 8). In addition, lanthanides enhanced catalytic performance and electrolyte cycling, which ultimately improved DSSC efficiency by 9.12% ($\eta = 7.30\%$) with a J_{sc} value of 18.44 mA cm^{-2} .

5. Lanthanide-doped nanomaterials in perovskite solar cells

Perovskite solar cells (PSCs) have emerged as a new field of dye-sensitized photovoltaics given its rapid advancements and material merits. Typical DSSCs require thick films of dyes ($\sim 10 \mu\text{m}$) for sufficient light absorption,¹⁵⁹ but solution processing can only achieve semiconductor films at a fraction, typically less than $1 \mu\text{m}$. Furthermore, by modifying perovskite compositions (A: Cs, Rb, FA, MA; B: Pb, Sn; and X: Cl, Br, I), absorbance can be tuned from the visible to the NIR-I region. High-performance panchromatic PSCs are technically possible with FASnI_3 ,¹⁶⁰ but this material is constrained by the inevitable oxidation of Sn^{2+} to Sn^{4+} and the cubic-to-orthorhombic phase

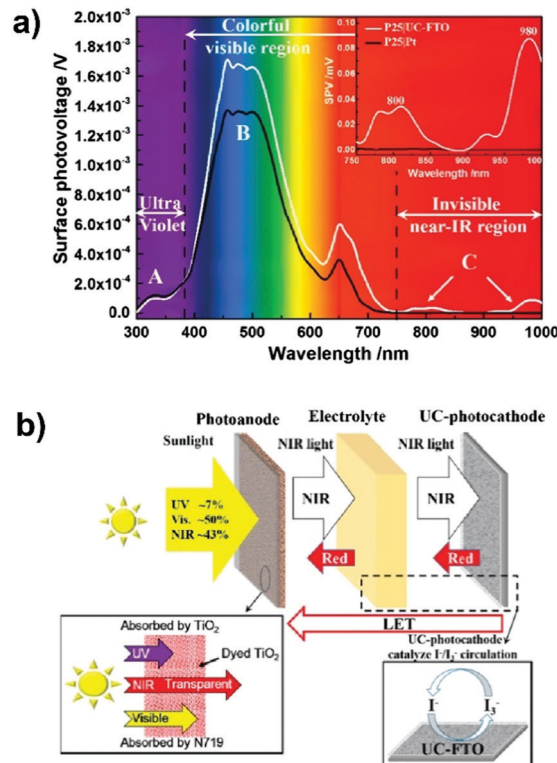


Fig. 8 (a) The surface photovoltage spectrum of a DSSC that is installed Pt counter electrode (black) and UC-FTO as the counter electrode (white) spanning over 300–1000 nm. Inset highlights the near-infrared (NIR) region between 750 and 1000 nm, as further evidence that the presence of Yb and Er dopants are directly responsible for the PV response in the NIR region. (b) An illustration of the photonic process of the DSSC equipped with the alternative UC-FTO nanoparticles that serves as the counter electrode. (Reproduced with permission from ref. 158, copyright 2014, American Chemical Society.).

transformation of metastable iodide perovskites. Therefore, photovoltaic management for sub-bandgap photons beyond 800 nm is an opportunity to be explored. As with DSSCs, upconversion integration into PSCs through judicious incorporation of lanthanide-doped materials is viable (Fig. 9).

With recent technological improvements, PSCs today are markedly different from DSSCs in terms of cell structure. Currently two designs are heavily adopted for research and development, namely mesoporous and planar perovskite solar cells. From a performance standpoint, a PSC that consists of an electron transport layer (ETL) of both compact and mesoporous scaffolds performs better than its planar, single-layer counterpart,^{161,162} but planar solar cells are attractive for flexible PVs due to simple processing steps and minimized material requirements.¹⁶³ A direct method to determine UC contribution is to apply an external upconverter.¹⁶⁴ Despite the simplicity, the results and data indicated that UC contribution and its exponential enhancement are only apparent under concentrated solar fluxes. In general, using concentrated solar fluxes for DSSCs and PSCs are avoided because high power pumping tends to fill deep trap states and complicates charge transport.¹⁶⁵ As such, there are three other possible approaches to integrate upconversion nanomaterials

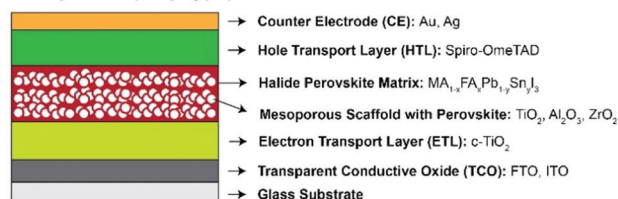
Mesoporous (n-i-p type)**Planar (n-i-p type)**

Fig. 9 A simplified schematic of the two main types of PSC architectures that are actively utilized in photovoltaic research. The first type is the meso-superstructured solar cell (Top) and the other is the planar, thin-film solar cell (Bottom). The heterojunction of both devices can be configured between the regular (n-i-p) or the inverted (p-i-n) archetypes, with respective material changes to HTL and ETL.

within the PSC structure for more effective enhancement: developing photoactive perovskites, employing an ETL that encompasses a compact, mesoporous scaffold, and using a hole transport layer (HTL).

5.1 Integrating lanthanide-doped nanomaterials into photoactive perovskite layer in PSCs

For planar PSCs, the absence of a mesoporous scaffold stresses the need for direct UCNP integration into perovskite layers (Table 4). An easy method is to sandwich UCNPs between the perovskite and the ETL or HTL, in which nanoparticles primarily function as UC emitters or achieve light scattering, with modest efficiency enhancements between 5 and 15.2%.^{166,167}

A second method is to adapt the quantum-dot-in-perovskite (QDiP) strategy developed by Sargent and co-workers.¹⁷⁰ Oleylamine- or oleate-capped UCNPs synthesized in a non-polar phase first underwent ligand exchange with perovskite precursors in a polar phase to generate a MAI-capped UCNPs. These MAI-capped UCNPs were then dispersed into a halide perovskite precursor solution before spin-coating to form UCNP-in-perovskite solids (Fig. 10). Meng *et al.*¹⁶⁸ demonstrated that such perovskite-UCNP hybrid films resulted in 54.4% efficiency enhancement. The large increment was attributed to the combined effect of bright UC emission, enabled by suppressed surface quenching of UCNP centers in the perovskite matrix, and the formation of highly crystalline and pinhole-free films. To enhance the spectral

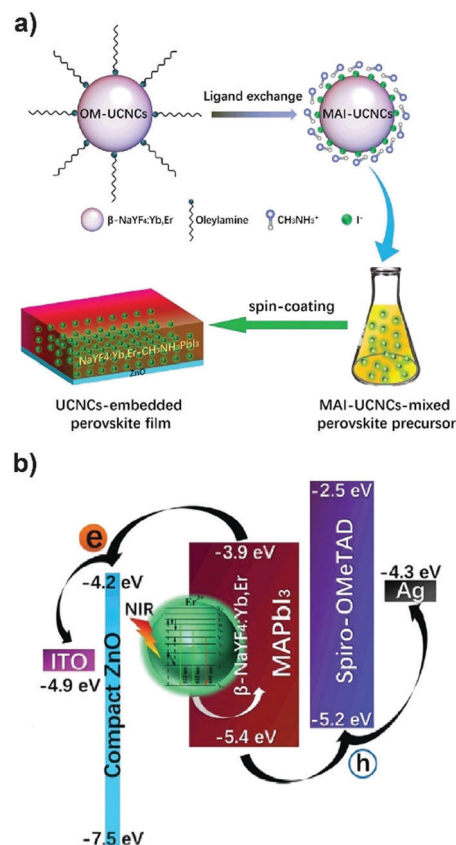


Fig. 10 (a) Schematic of the preparation of UCNP-in-perovskite films via a ligand-exchange process, followed by adding perovskite precursors. (b) Energy Schematic diagram illustrating the photovoltaic process and the UC energy transfer within a UCNPs-embedded planar PSC device. (Reproduced with permission from ref. 168, copyright 2017, Royal Society of Chemistry.).

response in the range of 800–1000 nm, Lai *et al.*¹⁶⁹ incorporated the perovskite matrix with IR806-sensitized UCNPs. However, the efficiency enhancement decreased to 29.4%, and the UCNP loading tolerance was reduced to 6 mg mL⁻¹, compared with 20 mg mL⁻¹ reported in the previous work. It is likely that surface-anchored dye molecules disrupt the quasiepitaxial interface between UCNPs and the perovskite matrix, which inevitably generates charge-trapping defects.¹⁷¹

5.2 Integrating lanthanide-doped nanomaterials into electron transport layers in PSCs

As with photoanodes in DSSCs, the ETL in PSCs is one of the most researched areas for improved PV performance.

Table 4 Summary of various UC phosphors used in the PSC photoactive layer, its solar cell structure, sensitizing perovskite composition and their contributions to the improvement (based on η metric) of photovoltaic devices

Upconversion phosphors	Device structure	Perovskite Composition	J_{sc} (mA cm ⁻²)	η (%)	Enhancement (%)	Ref.
NaYF ₄ :18%Yb/0.5%Tm	Planar (n-i-p)	CS _{0.05} (MA _{0.17} FA _{0.83}) _{0.95} PbI _{2.5} Br _{0.5}	25.45	18.20	15.20	166
KY ₂ F ₂₂ :20%Yb/5%Er	Planar (n-i-p)	FA _{0.79} CS _{0.05} MA _{0.16} PbI _{2.5} Br _{0.5}	20.10	16.80	5.00	167
	Planar (n-i-p), ETL-free	FA _{0.83} CS _{0.17} Pb(I _{0.6} Br _{0.4}) ₃	18.50	14.00	6.10	167
NaYF ₄ :20%Yb/2%Er	Planar (n-i-p)	MAPbI ₃	22.71	18.60	54.4	168
NaYF ₄ :20%Yb/2%Er	Planar (n-i-p)	MAPbI ₃	21.96	17.49	29.40	169

While TiO_2 is translatable from DSSCs to PSCs as an n-type ETL material, it presents unique challenges when assembled with halide perovskites. First, the desorption of oxygen from TiO_2 upon UV exposure can accelerate the decomposition of air-sensitive perovskites, limiting their operational lifetime.¹⁷² Second, unlike dyes that simply function as sensitizers in DSSCs, perovskites can function as hole transporters and absorbers, or electron transporters.¹⁷³ Hence, charge mobilities between the ETL-perovskite-HTL must be compatible. Pristine TiO_2 possesses a lower electron mobility ($10^{-5} \text{ cm}^2 \text{ V}^{-1} \text{ s}^{-1}$) than the perovskite ($60 \text{ cm}^2 \text{ V}^{-1} \text{ s}^{-1}$) and Li^+ -doped Spiro-OmeTAD ($10^{-3} \text{ cm}^2 \text{ V}^{-1} \text{ s}^{-1}$).^{174,175} The imbalanced charge transport results in space charge-limited photocurrents and hysteresis.¹⁷⁶ Moreover, the energy levels of TiO_2 and perovskites in PSCs are not perfectly aligned, compounded by interfacial charge barriers between them.¹⁷⁷ Inefficient charge transfer and accumulation at deep trap sites causes unwanted radiative recombination, another technical obstacle that prevents high conversion efficiency. Within a short span of 5 years, almost all lanthanides have been introduced into both mesoporous and compact layers of TiO_2 with varying degrees of enhancement (Table 5).

Incorporating lanthanide ions into the scaffold layer of mesoporous PSCs has been explored *via* two general methods. The first method is direct doping by adding lanthanide precursors during synthesis. Gao *et al.* reported an efficiency enhancement of 28.8% using La^{3+} as the dopant because of its oxyphilic nature to metal oxides and its lack of energy levels to interfere electronic transport.¹⁷⁸ They claimed that the main contribution to enhanced efficiency comes from a change in the Fermi energy of TiO_2 , creating oxygen vacancies and enhancing the V_{OC} of PSCs. However, these solar cells are more prone to damage and substantial energy loss under UV exposure. Subsequently, Nd^{3+} -doping was attempted by Roose *et al.* to mitigate the photocurrent loss

inherent to Al^{3+} -doping.¹⁷⁹ Nd^{3+} -doping at the surface showed reduction in the density of deep trap states at the perovskite- TiO_2 interface. This prevented recombination, induced faster electron transport, and increased the stability of PSCs. Moreover, Ren *et al.* discovered that Er^{3+} -doping into TiO_2 can induce similar effects upon controlled formation of a mixed crystalline rutile/anatase phase (Fig. 11).¹⁸⁰ By careful control of the rutile phase composition that is responsible for charge recombination, the composite further accelerated electron extraction, while suppressing photo-induced holes in TiO_2 . This strategy has also been extended to Eu^{3+} and Er - Yb - Li doping for UC evaluation, yielding similar conclusions.^{181,182}

The second method is to incorporate lanthanide-doped nanoparticles into mesoporous scaffolds. However, as lanthanides are not directly coupled to the TiO_2 lattice at the atomic level, their main roles are to harvest NIR light for UC and to serve as light scattering centers for enhanced light absorption. To this end, UC lanthanide-ion pairs, such as Yb/Er , Yb/Ho and Yb/Tm , have been applied.^{183–187} Since the UC emission contribution to PVs is intrinsically low compared to halide perovskites, several enhancement strategies have been explored. For instance, Guo *et al.* doped Sc^{3+} into $\text{NaYF}_4:\text{Yb}/\text{Er}$ core-shell UCNPs to form an additional energy transfer channel, augmenting the green emission by several folds.¹⁸⁸ This UCNP design improved the efficiency of PSCs from 15.8 to 20.19%. To amplify the absorption between 800–1000 nm, Zhou *et al.* synthesized Er_2O_3 nanocomposites that incorporate Cu_{2-x}S as an infrared antenna.¹⁸⁹ As a result, emission intensity from UCNPs increased by three orders of magnitude, boosting the PSC efficiency from 10 to 17.80%. However, given the reduced thickness of the TiO_2 layer in PSCs for effective charge transport, less UCNPs can be loaded into the TiO_2 layer, thus compromising the extent of UC and light scattering.

Table 5 Summary of various lanthanide dopants and lanthanide-doped nanomaterials used in the ETL layer, its solar cell structure, sensitizing perovskite composition and their contributions to the improvement (based on η metric) of photovoltaic devices

ETL material	Device structure	Perovskite Composition	J_{sc} (mA cm^{-2})	η (%)	Enhancement (%)	Ref.
$\text{TiO}_2:\text{La}$	Mesoporous (n-i-p)	MAPbI_3	21.30	14.23	27.33	178
$\text{TiO}_2:\text{Nd}$	Mesoporous (n-i-p)	$\text{FA}_{0.83}\text{MA}_{0.17}\text{PbI}_{2.5}\text{Br}_{0.5}$	22.30	18.10	4.63	179
$\text{TiO}_2:\text{Er}$	Mesoporous (n-i-p)	MAPbI_3	20.28	14.06	45.85	180
$\text{TiO}_2:\text{Eu}$	Mesoporous (n-i-p)	MAPbI_3	22.62	17.90	12.93	181
$\text{TiO}_2:\text{Yb}/\text{Er}/\text{Li}$	Mesoporous (n-i-p)	$\text{Cs}_{0.05}(\text{MA}_{0.17}\text{FA}_{0.83})_{0.95}\text{PbI}_{2.5}\text{Br}_{0.5}$	22.20	16.50	17.86	182
$\text{TiO}_2-\text{NaYF}_4:49\% \text{Yb}/1\% \text{Tm}$	Mesoporous (n-i-p)	MAPbI_3	21.70	16.90	20.00	183
$\text{NaYF}_4:20\% \text{Yb}/2\% \text{Er}$	Mesoporous (n-i-p)	MAPbI_3	22.14	17.80	2.26	184
$\text{TiO}_2-\text{NaYF}_4:49\% \text{Yb}/1\% \text{Tm}/\text{SiO}_2$	HTL-Free, carbon electrode	MAPbI_3	21.43	14.09	12.92	185
$\text{TiO}_2-\text{NaYF}_4:20\% \text{Yb}/2\% \text{Er}$	Mesoporous (n-i-p)	MAPbI_3	20.23	15.98	13.74	186
$\text{ZrO}_2-\text{NaYbF}_4:\text{Ho}$	HTL-Free, carbon electrode	$\text{FA}_{0.4}\text{MA}_{0.6}\text{PbI}_3$	25.16	14.32	28.80	187
$\text{TiO}_2-\text{NaYF}_4:20\% \text{Yb}/2\% \text{Er}/8\% \text{Sc}$	Mesoporous (n-i-p)	$\text{Cs}_{0.05}(\text{FA}_{0.83}\text{MA}_{0.17})_{0.95}\text{Pb}(\text{I}_{0.9}\text{Br}_{0.1})_3$	22.91	20.19	15.77	188
$\text{TiO}_2:13\% \text{Er}/6\% \text{Yb}$	Planar (n-i-p)	$\text{MAPbI}_{3-x}\text{Cl}_x$	21.70	12.90	25.24	190
$\text{TiO}_2:\text{Sm}$	Planar (n-i-p)	MAPbI_3	18.07	13.10	10.46	191
$\text{TiO}_2:\text{Eu}$	Planar (n-i-p)	$\text{Cs}_{0.05}\text{FA}_{0.80}\text{MA}_{0.15}\text{Pb}(\text{Br}_{0.85}\text{I}_{0.15})_3$	23.32	20.13	8.34	192
$\text{TiO}_2:\text{La}$	Planar (n-i-p)	MAPbI_3	21.80	15.50	16.54	193
$\text{TiO}_2:\text{Gd}$	Planar (n-i-p)	$\text{Cs}_{0.04}\text{FA}_{0.80}\text{MA}_{0.16}\text{Pb}(\text{Br}_{0.85}\text{I}_{0.15})_3$	22.82	19.60	3.21	194
$\text{SnO}_2:\text{La}$	Planar (n-i-p)	MAPbI_3	21.77	17.08	19.94	196
$\text{BaSnO}_3:\text{La}$	Mesoporous (n-i-p)	MAPbI_3	23.00	21.20	7.61	198
$\text{CeO}_{1.87}$	Mesoporous (n-i-p)	MAPbI_3	21.44	13.77	−9.41	201
CeO_x	Mesoporous (n-i-p), PCBM	MAPbI_3	22.90	16.85	10.86	201
	Planar (p-i-n)	MAPbI_3	19.90	16.10	—	203
	Planar (p-i-n), PCBM	MAPbI_3	20.94	16.70	—	202
$\text{ZnO}-\text{CeO}$	Mesoporous (n-i-p)	MAPbI_3	23.64	19.52	21.92	204

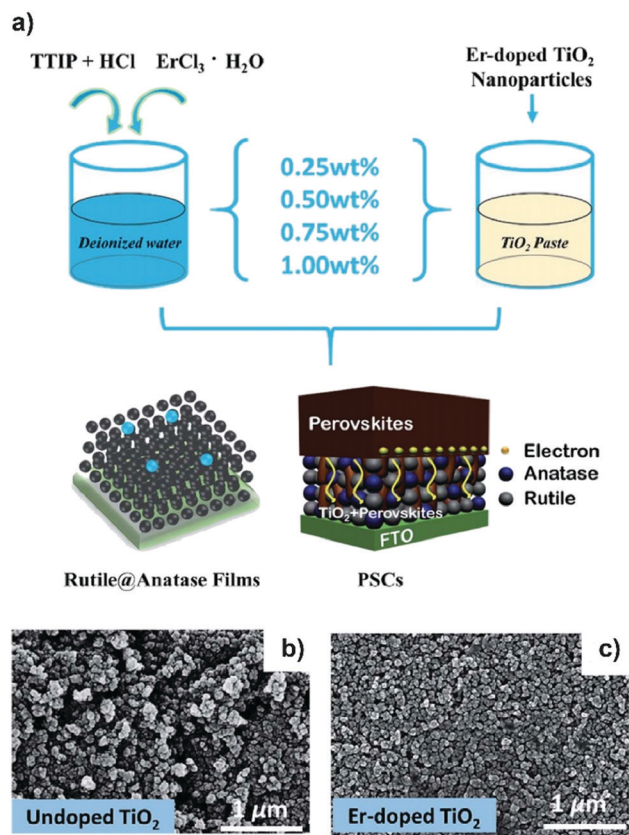


Fig. 11 (a) Schematic illustration of the fabrication of the PSCs with Er-doped TiO₂ films. (b) SEM images of undoped TiO₂ and (c) Er-doped TiO₂ film with substantial improvement in film morphology. (Reproduced with permission from ref. 180, copyright 2018, Royal Society of Chemistry.).

Considering the potential of planar PSCs for various applications, doping lanthanides into compact TiO₂ layers is also of considerable research interest.^{190–193} For instance, Chen *et al.* doped a series of lanthanides into a compact TiO₂ layer and verified that La, Gd and Nd dopants exhibited positive effects on the PSC performance, whereas heavier dopants, such as Yb, Tm and Lu, performed worse. While their results concur with previous studies, the impact of other dopants, such as Ho, Dy and Pr, remains ambiguous because their investigations only cover 8 out of the 14 lanthanides.¹⁹⁴

Although lanthanide doping is a versatile option, many studies have achieved doping only at low concentrations (0.5–2.5%). Higher doping contents cause interstitial doping, which forms trap states that hampers the PSC performance. While there are improvements in electron mobility, it is insignificant compared with perovskites and the HTL layer. Hence, total replacement of TiO₂ is the other viable option. In search of alternatives, the material should possess the following characteristics: (i) aligned energy levels with perovskites for efficient charge transfer and hole blocking, (ii) high electron mobility, (iii) high optical transmittance (*e.g.*, wide optical bandgaps), (iv) stability for long-term performance, and (v) mild processing conditions.¹⁹⁵ One of the most promising candidates is SnO₂, which fulfills all above requirements. However, formation of

compact SnO₂ films with low defect density requires mild annealing conditions since SnO₂ tends to aggregate spontaneously. To tackle this problem, Xu *et al.* demonstrated that La-doping can influence the crystallization of SnO₂ during annealing, yielding high-quality films.¹⁹⁶ When La-doping was applied to a mesoporous scaffold of SnO₂, the dopant facilitated the formation of dense, large perovskite crystals.

Another candidate is La-doped BaSnO₃. This material was not initially considered for use in PSCs due to challenges in low-temperature synthesis.¹⁹⁷ Eventually, Shin *et al.* managed to synthesize La-doped BaSnO₃ nanoparticles in crystalline superoxide molecular clusters under ambient conditions.¹⁹⁸ When applied as a mesoporous layer in PSCs, these nanoparticles achieved an efficiency of 21.3% and long-term operational stability over 1000 h. Moreover, BaSnO₃ exhibited a high doping threshold for La owing to its cubic perovskite crystal structure. This crystal structure enabled better band alignment and electron transport without compromising the stability of PSCs.¹⁹⁹

Among various lanthanide oxides, CeO₂ has received considerable attention as a suitable ETL. CeO₂ stands at an advantage over other lanthanide oxides because of its ease of access, high photostability, facile modulation in conduction band, making it ideal for photocatalysis.²⁰⁰ However, it has some limitations associated with application for PSCs. For instance, Wang *et al.* showed that as-synthesized CeO_x (1.50 < *x* < 2.00) mesoporous scaffolds were of poor quality due to the formation of amorphous films and large islands.²⁰¹ To improve charge transport and electron extraction, PC₆₁BM or C₆₀ as an interfacial modification could be introduced, with an efficiency enhancement of 10.9%.²⁰² More recently, CeO_x was utilized as an ETL material for inverted heterojunction PSCs.^{203,204} However, the electronic and defect properties of CeO_x are not well understood. Compared with other ETLs, CeO_x-based PSCs display modest PV performance.

5.3 Integrating lanthanide-doped nanomaterials into hole transport layers in PSCs

For n-i-p heterojunction PSCs, Spiro-OMeTAD is a crucial HTL material for achieving the best performance. By virtue of its organic composition, Spiro-OMeTAD is often doped with organic additives and molecules, but is less tolerant of inorganic moieties such as nanoparticles.²⁰⁵ For instance, Xu *et al.* attempted to incorporate NaCsWO₃@NaYF₄@NaYF₄:Yb/Er UCNPs into the HTL layer of PSCs with only ~0.1% of the nanofillers.²⁰⁶ Nonetheless, the incorporation of UCNPs raised device efficiency by 18%, which was attributed to a combined contribution of plasmon-enhanced UC emission and the partial improvement in the perovskite's surface morphology. Meanwhile, Ding *et al.* synthesized NaYF₄:Yb/Er/Li-Ag@SiO₂ nanocomposites with a maximum UCNP load capacity of 12 mg mL⁻¹, which increased the PSC device efficiency from 7.83 to 9.84%.²⁰⁷

For inverted p-i-n-type heterojunction PSCs, NiO is often used as an inorganic HTL material owing to its low-temperature processing, negligible hysteresis, and its superior stability.²⁰⁸ As with TiO₂, the use of NiO is hindered by its low intrinsic conductivity.²⁰⁹ Although NiO is often doped with noble metals

as p-type dopants with similar ionic radii, recent studies have shown that it is possible to dope lanthanides into NiO. For instance, upon doping of 3 mol% La^{3+} into a NiO_x matrix, Teo *et al.* observed passivation of trap states with improved film quality, yielding an efficiency of 15.03%.²¹⁰ The addition of La^{3+} also imparted remarkable stability to the device, retaining 95% of its efficiency after storage for 50 days. In a separate development, Song and co-workers investigated doping of several types of lanthanides (Ce, Nd, Eu, Tb, Yb) into NiO_x , which exhibited varying degrees of improvements in PCE performance, with Eu being the most effective p-type dopant.²¹¹

5.4 Lanthanide doping in perovskites – improved stability and performance

Unlike DSSCs, the cubic crystalline structure of halide perovskites makes possible to substitute lead centers with lanthanides at certain doping levels. Indeed, suitable conditions, such as compatible ionic radii and the octahedron coordination environment, often allow relative ease of lanthanide doping up to 10 wt%.⁴⁷ Of particular interest is Eu, for which Miyasaka and co-workers observed that this dopant can significantly retard the α -to- δ phase transformation of CsPbI_3 (Fig. 12a).²¹² The constructed PSCs achieved 6.8% efficiency and could withstand ambient conditions for more than 30 days. Subsequently, Wang *et al.*²¹³ proposed that the key role of Eu in perovskites is to create a redox shuttle between Eu^{3+} and Eu^{2+} states, which simultaneously eliminates Pb^0 and I^0 defects (Fig. 12b). This redox reaction is self-sustaining and provides a solution for durable PSCs, as evidenced by the remarkable efficiency of

21.52% and their abilities to retain 92% of efficiency even under AM1.5G illumination for 1500 hours.

Apart from Eu, Yb can improve the stability of iodide perovskites. Its precursor, YbCl_3 is added to serve two functions: increase the tolerance factor of CsPbI_3 by substituting Pb for lattice shrinkage and form an adduct complex of $\text{YbCl}_3 \cdot \text{DMSO}$, the additive can passivate the pinholes of the perovskite film, thus improving the perovskite crystalline quality. To date, Wang *et al.*²¹⁴ have demonstrated that PSCs based on $\text{YbCl}_3/\alpha\text{-CsPbI}_3$ can increase efficiency from 9.3% to 11.4%. As demonstrated in the work of Miyasaka and co-workers, PCE was expected to raise further with optimized cells. Moreover, considering the recent success in the synthesis of CsYbI_3 , albeit in the form of colloidal quantum dots,²¹⁵ there is a possibility to alloy CsPbI_3 with Yb^{2+} for achieving stable perovskites and long-lasting PSCs. This direction of research is still at its infancy and we anticipate more lanthanides, particularly Er and Tm, to be studied in the iodide perovskite matrix in the future.

6. Perspectives and future developments

While lanthanide-doped materials have not been successful as UC phosphors in commercial C-Si PVs, these materials have enabled DSSCs to achieve higher device efficiencies. Despite a better understanding of UC mechanisms, their involvement in improving photovoltaic performance remains minor in most DSSCs. Alternatively, incorporating lanthanides into the multi-component photovoltaic structure of DSSCs has proven beneficial in addressing its inherent design shortfalls. For instance, UC phosphors can serve as an internal light-scattering layer for better light capture. The design of UC- TiO_2 composites also expands the photoanode surface area, allowing increased dye loading and better solar harvesting. Trivalent lanthanide dopants also improve charge transport in the photoanode. For PSCs, lanthanide doping is particularly useful in addressing technical limitations. We have also seen some cases where UC phosphors can be incorporated in the counter electrode of DSSCs to promote electrolyte cycling.

In addition, downconversion lanthanide-based phosphors,^{216,217} when applied internally, can also preserve the electrolyte stability of the DSSC device by mitigating damage from ultraviolet radiation. Sub-micron or nanoscale level lanthanide-doped materials have secondary functions that complement photonic upconversion in PV application.²¹⁸ An external application of UC phosphors as spectral converters only results in limited improvements. Though rarely mentioned, UC phosphors as external spectral converters are further hindered by signal attenuation due to interfacial reflection and scattering.²¹⁹

Another observation is that the application of UC phosphors to PV materials with larger bandgaps tends to give larger enhancements in efficiency (Table 6). This is because large-bandgap PVs typically have low efficiencies due to limited spectral capture of the solar spectrum (Fig. 13). This indicates that PV platforms ($E_g > 1.50$ eV), such as DSSCs and organic/amorphous silicon, tend to benefit more through UC compared with PSCs or C-Si PVs. Notably, the eventual performance of PVs also depends on other

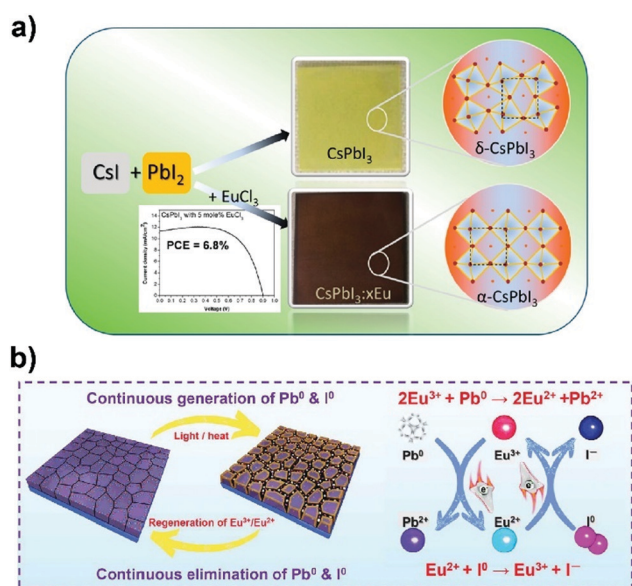


Fig. 12 (a) Illustration of the Eu-doping effect on the perovskite stability. The most obvious effect is the prolonged phase stabilization of the black cubic phase, a long-standing problem in PSCs. (b) Proposed mechanism diagram as an effect of Eu-doping, it kickstarts a cyclical elimination of Pb^0 and I^0 defects while regenerating Eu^{3+} – Eu^{2+} ion pair (Reproduced with permission from ref. 212 and 213, copyright 2018 and 2019, American Chemical Society and American Association for the Advancement of Science.).

Table 6 A summary of existing photovoltaic technologies, featuring different bandgaps, fractions of incident sub-bandgap photons, their associated power losses, and efficiencies achieved from best-performing devices. All technologies are evaluated as single-junction terrestrial cells and submodules at 25 °C under the global AM 1.5G (1000 W m⁻²)

Photovoltaic technology	Bandgap (eV)	Fraction of sub-bandgap photons (%)	Fraction of power carried by sub-bandgap photons (%)	Efficiency of best-performing device (%)
Crystalline silicon	1.12	36.3	19	26.7
Gallium Arsenide (thin-film)	1.42	53.5	34	29.1
CIGS (thin-film)	1.14–1.40	37–55	19–35	23.4
Perovskite	1.50	58	39	21.6
Organic	1.77–1.91	70–76	52–59	15.2
Dye-sensitized	1.65	65	46	11.9
Amorphous silicon	1.70	68	49	10.2

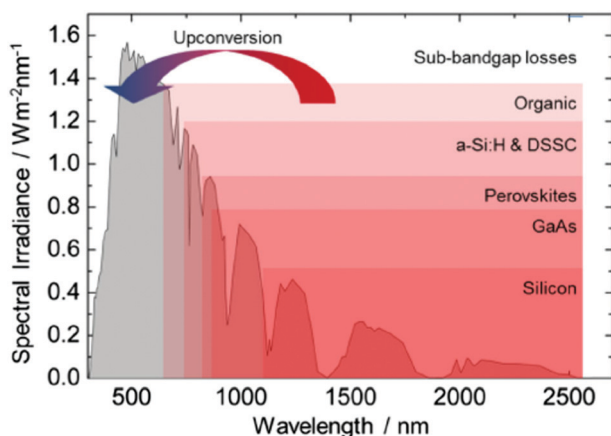


Fig. 13 An AM 1.5G spectrum that is overlapped by regions of the spectrum where the respective PVs suffer from transmission losses due to sub-bandgap photons. The regions in different degrees of red indicate the wavelengths where UC can be used to reabsorption by the PV module. (Reproduced with permission from ref. 60, copyright 2015, Wiley-VCH Verlag GmbH & Co. KGaA).

factors, such as the maturity of PV technology and the sensitivity of the primary absorbing PV material to the solar spectrum.¹³⁶

Notwithstanding many advances, several challenging issues remain for DSSCs and other alternative PVs. Indicative from Table 1 and 2, UC material enhancement has yet to push a majority of DSSC devices beyond 10% conversion efficiency.¹⁴¹ While conversion efficiency can be pushed further with strategies such as simultaneous spectral conversion, one of the problems is that most UC phosphors have a narrow solar harvesting spectrum in the NIR region, limiting photon conversion.²²¹ Therefore, efforts have been channeled to incorporate multiple lanthanide ions into the upconverter material host matrix for broadband excitation while mitigating self-quenching. Core-multilayer-shell structures have been proposed, with NIR-absorbing lanthanides incorporated into shell layers to harvest different spectral regions.^{220,222,223} It has been proven feasible to cover the NIR-II and NIR-III regions with Er, Tm, and Ho, beyond the commonly used Yb- and Nd-based sensitizers. However, the major challenge lies in the simultaneous accommodation of multiple lanthanides in a single nanoparticle structure to derive the best possible UC effect for PVs (Fig. 14 and 15).

The inherently low QY of lanthanide-doped UC materials under AM 1.5G conditions adversely impacts the improvement

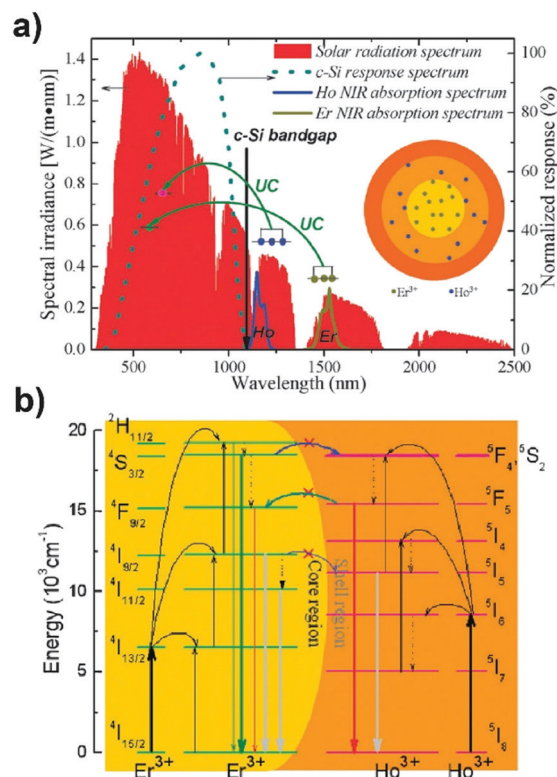


Fig. 14 (a) Schematic in the AM1.5G curve of how NIR light, which is transparent to C-Si/DSSCs, can be upconverted into visible light through the design of NaGdF₄:Er@NaGdF₄:Ho@NaGdF₄ nanoparticles. (b) Energy level diagram of how Er and Ho ions can perform possible energy transfer processes based on the design of the nanoparticles in a) and how the core-shell interface can mitigate cross-relaxation caused by energy transfer from Er to Ho. (Reproduced with permission from ref. 220, copyright 2012, Royal Society of Chemistry.).

of DSSCs or any other types of PVs. For C-Si PVs, using solar concentrators can create high power density and facilitate efficient UC *via* ETU. In contrast, solar concentrators are less feasible for DSSCs as high power will degrade the sensitizers and the electrolyte. Therefore, co-sensitization is perhaps the most promising method to address the low absorption coefficient of lanthanides while allowing broadband UC. For instance, Chen *et al.*²²⁴ demonstrated its feasibility with a dye (IR783) complementary to both UCNPs and the N719 dye in DSSCs, achieving an efficiency enhancement of 13.1%. However, a major constraint is

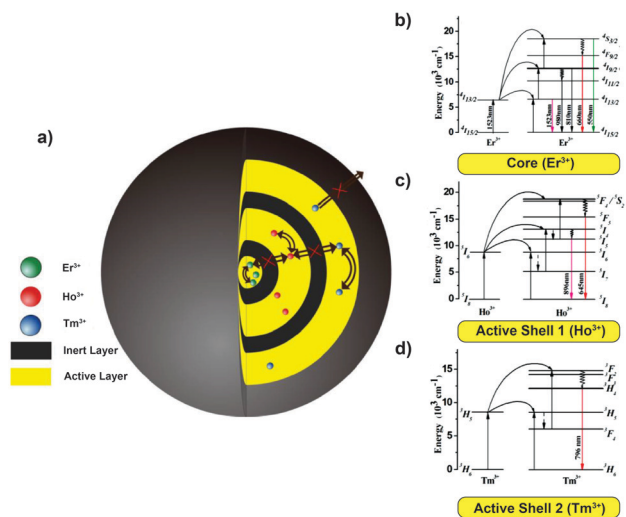


Fig. 15 (a) Schematic design of the giant multi-layered $\text{NaYF}_4:10\%\text{Er}@\text{NaYF}_4:10\%\text{Ho}@\text{NaYF}_4:1\%\text{Tm}@\text{NaYF}_4$, with inert intermediate layers used to isolate activators and prevent cross-relaxation. The proposed ETU processes in the constituent active layers are demonstrated in (b) Er–Er, (c) Ho–Ho and (d) Tm–Tm based systems, respectively. (Reproduced and adapted with permission from ref. 222, copyright 2015, Wiley-VCH Verlag GmbH & Co. KGaA.).

the lack of NIR dyes with absorption beyond the 900 nm range, which renders this approach untenable for NIR-II and NIR-III regions. Nonetheless, with the newly studied mechanics of lanthanide–dye molecule coupled upconversion, it might be possible to overcome the constraints by tapping into triplet states of the dyes, which have much longer wavelength cut-off than their singlet states. Within the proximity of $\text{NaGdF}_4:\text{Ln}$ nanoparticles, the low-energy triplet states of dyes can be excited directly, bypassing their high-energy singlet states for lanthanide sensitization.^{54,55}

Alternatively, growing a semiconductor shell over lanthanide-doped hosts presents an ideal solution as it confers material stability and surface passivation to enhance luminescence. In addition, a highly absorbing semiconductor shell can be considered as an alternative sensitizer to organic dyes and chromophores, enabling energy transfer to lanthanide ions in the core. For instance, a recent achievement was done by Gao *et al.*, who managed to synthesize $\text{KMnF}_3:\text{Yb}/\text{Er}@\text{ZnS}$ nanoparticles *via* direct epitaxial growth sites.²²⁵ While there was a marked improvement in UC luminescence under 980 nm excitation, the direct contribution of the semiconductor sensitization was unaddressed, and the increased emission was possibly due to passivation of surface quenching sites. The lack of actual QY values is also an ambiguity that does not address the semiconductor role either. Meanwhile, it will be interesting to study the difference in UC emission between a wide bandgap semiconductor shell (*e.g.*, ZnS, InP, or CdS) and a small bandgap shell (*e.g.*, PbS), but growing these epitaxial shells may pose a synthetic challenge.

7. Conclusions

Although the use of lanthanide-doped UC materials to improve DSSC performance has only been under the spotlight for the

past decade, we have witnessed more progress compared with crystalline silicon solar cells. This can be attributed to the structural flexibility of DSSCs, to which lanthanide-doped materials can be conveniently coupled. Thus far, UC phosphors have proven the most effective when applied internally in the photoanode or externally as a scattering layer, whereby their upconverting capabilities can be improved by coupling with surface plasmon resonance, while detrimental charge recombination can be alleviated by surface coating with NaYF_4 , SiO_2 or TiO_2 inert shells. The degree of PV performance improvement would ultimately depend on the lanthanide UC efficiency, the scattering property of the phosphors and lanthanide absorption capacity. We expect more work to focus on efficiency improvements in the near future by using better materials or alternative UC mechanisms.

In one way or another, most of the UC concepts that were previously conceived and tried on crystalline solar cells were also applied to DSSCs. During the processes of translation, minor adaptations must be made, considering their differences in cell architecture. However, UC phosphors, especially nanoparticles, have proven ideal for structural modification to create multifunctional materials in addition to producing upconverted light. This suggests that they are also amenable to other photovoltaic concepts. For instance, UCNPs have begun to be applied to halide PSCs that share a similar photovoltaic structure with DSSCs. Given the semiconducting nature of halide perovskites, incorporating lanthanides into their crystalline structures offers even more possibilities. While lanthanides in photovoltaics are often associated with upconversion output in the past, they are now also considered as tools to develop high quality and long-lasting PSCs. Developing lanthanide-doped materials for enhanced photovoltaics remains a promising field for identifying problems and shortcomings, choosing suitable photovoltaic platforms, and devising high-performance materials.

Conflicts of interest

There are no conflicts to declare.

Acknowledgements

This work is supported by Agency for Science, Technology and Research (A*STAR) under its AME program (Grant NO. A1883c0011 and A1983c0038), National Research Foundation, the Prime Minister's Office of Singapore under its NRF Investigatorship Programme (Award No. NRF-NRFI05-2019-0003), and the GSK-EDB Trust Fund Program through SIMTech (R143000698504).

Notes and references

- 1 A. de Vos, *J. Phys. D: Appl. Phys.*, 1980, **13**, 839–846.
- 2 R. A. S. Ferreira, S. F. H. Correia, A. Monguzzi, X. Liu and F. Meinardi, *Mater. Today*, 2020, **33**, 105–121.
- 3 T. Trupke, M. A. Green and P. Würfel, *J. Appl. Phys.*, 2002, **92**, 4117–4122.

- 4 A. Shalav, B. S. Richards, T. Trupke, K. W. Krämer and H. U. Güdel, *Appl. Phys. Lett.*, 2005, **86**, 013505.
- 5 P. Ramasamy, P. Manivasakan and J. Kim, *RSC Adv.*, 2014, **4**, 34873–34895.
- 6 D. Li, H. Ågren and G. Chen, *Dalton Trans.*, 2018, **47**, 8526–8537.
- 7 N. Yao, J. Huang, K. Fu, X. Deng, M. Ding and X. Xu, *RSC Adv.*, 2016, **6**, 17546–17559.
- 8 F. Auzel, *Chem. Rev.*, 2004, **104**, 139–173.
- 9 T. N. Singh-Rachford and F. N. Castellano, *Coord. Chem. Rev.*, 2010, **254**, 2560–2573.
- 10 G. Chen, H. Qiu, P. N. Prasad and X. Chen, *Chem. Rev.*, 2014, **114**, 5161–5214.
- 11 F. Wang and X. Liu, *Chem. Soc. Rev.*, 2009, **38**, 976–989.
- 12 X. Huang, S. Han, W. Huang and X. Liu, *Chem. Soc. Rev.*, 2013, **42**, 173–201.
- 13 J. Zhou, Q. Liu, W. Feng, Y. Sun and F. Li, *Chem. Rev.*, 2015, **115**, 395–465.
- 14 Z. Wang and A. Meijerink, *J. Phys. Chem. C*, 2018, **122**, 26298–26306.
- 15 G. Chen, T. Y. Ohulchanskyy, A. Kachynski, H. Ågren and P. N. Prasad, *ACS Nano*, 2011, **5**, 4981–4986.
- 16 G. A. Kumar, M. Pokhrel and D. K. Sardar, *Mater. Lett.*, 2012, **68**, 395–398.
- 17 F. Auzel, *J. Lumin.*, 1990, **45**, 341–345.
- 18 K. Prorok, A. Bednarkiewicz, B. Cichy, A. Gnach, M. Misiak, M. Sobczyk and W. Strek, *Nanoscale*, 2014, **6**, 1855–1864.
- 19 F. W. Ostermayer and L. G. van Uitert, *Phys. Rev. B: Solid State*, 1970, **1**, 4208–4212.
- 20 Q. Zou, P. Huang, W. Zheng, W. You, R. Li, D. Tu, J. Xu and X. Chen, *Nanoscale*, 2017, **9**, 6521–6528.
- 21 C. Lee, E. Z. Xu, Y. Liu, A. Teitelboim, K. Yao, A. Fernandez-Bravo, A. M. Kotulska, S. H. Nam, Y. D. Suh, A. Bednarkiewicz, B. E. Cohen, E. M. Chan and P. J. Schuck, *Nature*, 2021, **589**, 230–235.
- 22 A. Khare, *J. Alloys Compd.*, 2020, **821**, 153214.
- 23 A. Shalav, B. S. Richards and M. A. Green, *Sol. Energy Mater. Sol. Cells*, 2007, **91**, 829–842.
- 24 F. Wang, R. Deng, J. Wang, Q. Wang, Y. Han, H. Zhu, X. Chen and X. Liu, *Nat. Mater.*, 2011, **10**, 968–973.
- 25 R. T. Wegh, H. Donker, K. D. Oskam and A. Meijerink, *Science*, 1999, **283**, 663–666.
- 26 X. Liu, X. Kong, Y. Zhang, L. Tu, Y. Wang, Q. Zeng, C. Li, Z. Shi and H. Zhang, *Chem. Commun.*, 2011, **47**, 11957–11959.
- 27 B. Zhou, L. Yan, L. Tao, N. Song, M. Wu, T. Wang and Q. Zhang, *Adv. Sci.*, 2018, **5**, 1700667.
- 28 N. Song, B. Zhou, L. Yan, J. Huang and Q. Zhang, *Front. Chem.*, 2019, **6**, 673.
- 29 J. Zuo, D. Sun, L. Tu, Y. Wu, Y. Cao, B. Xue, Y. Zhang, Y. Chang, X. Liu, X. Kong, W. J. Buma, E. J. Meijer and H. Zhang, *Angew. Chem., Int. Ed.*, 2018, **57**, 3054–3058.
- 30 L. Zhou, Y. Fan, R. Wang, X. Li, L. Fan and F. Zhang, *Angew. Chem., Int. Ed.*, 2018, **57**, 12824–12829.
- 31 B. Zhou, J. Huang, L. Yan, X. Liu, N. Song, L. Tao and Q. Zhang, *Adv. Mater.*, 2019, **31**, 1806308.
- 32 T. Sun, Y. Li, W. L. Ho, Q. Zhu, X. Chen, L. Jin, H. Zhu, B. Huang, J. Lin, B. E. Little, S. T. Chu and F. Wang, *Nat. Commun.*, 2019, **10**, 1811.
- 33 B. Zhou, L. Yan, J. Huang, X. Liu, L. Tao and Q. Zhang, *Nat. Photonics*, 2020, **14**, 760–766.
- 34 G. Blasse, *Mater. Chem. Phys.*, 1987, **16**, 201–236.
- 35 L. Yan, B. Zhou, N. Song, X. Liu, J. Huang, T. Wang, L. Tao and Q. Zhang, *Nanoscale*, 2018, **10**, 17949–17957.
- 36 C. Fan, L. Wei, T. Niu, M. Rao, G. Cheng, J. J. Chruma, W. Wu and C. Yang, *J. Am. Chem. Soc.*, 2019, **141**, 15070–15077.
- 37 Y. Y. Cheng, T. Khoury, R. G. C. R. Clady, M. J. Y. Tayebjee, N. J. Ekins-Daukes, M. J. Crossley and T. W. Schmidt, *Phys. Chem. Chem. Phys.*, 2010, **12**, 66–71.
- 38 M. J. Y. Tayebjee, D. R. McCamey and T. W. Schmidt, *J. Phys. Chem. Lett.*, 2015, **6**, 2367–2378.
- 39 A. Olesund, V. Gray, J. Mårtensson and B. Albinsson, *J. Am. Chem. Soc.*, 2021, **143**, 5745–5754.
- 40 J. E. Auckett, Y. Y. Chen, T. Khoury, R. G. C. R. Clady, N. J. Ekins-Daukes, M. J. Crossley and T. W. Schmidt, *J. Phys.: Conf. Ser.*, 2009, **185**, 012002.
- 41 X. Wang, R. Tom, X. Liu, D. N. Congreve and N. Marom, *J. Mater. Chem. C*, 2020, **8**, 10816–10824.
- 42 S. K. Sugunan, U. Tripathy, S. M. K. Brunet, M. F. Paige and R. P. Steer, *J. Phys. Chem. A*, 2009, **113**, 8548–8556.
- 43 S. Balushev, V. Yakutkin, G. Wegner, B. Minch, T. Miteva, G. Nelles and A. Yasuda, *J. Appl. Phys.*, 2007, **101**, 023101.
- 44 P. Bharmoria, H. Bildirir and K. Moth-Poulsen, *Chem. Soc. Rev.*, 2020, **49**, 6529–6554.
- 45 N. Kiseleva, P. Nazari, C. Dee, D. Busko, B. S. Richards, M. Seitz, I. A. Howard and A. Turshatov, *J. Phys. Chem. Lett.*, 2020, **11**, 2477–2481.
- 46 W. Wei, G. Chen, A. Baev, G. S. He, W. Shao, J. Damasco and P. N. Prasad, *J. Am. Chem. Soc.*, 2016, **138**, 15130–15133.
- 47 R. Marin and D. Jaque, *Chem. Rev.*, 2021, **121**, 1425–1462.
- 48 L. Sun, R. Gao, T. Pan, X. C. Ai, L. Fu and J. P. Zhang, *Nanoscale*, 2019, **11**, 18150–18158.
- 49 W. Shao, G. Chen, A. Kuzmin, H. L. Kutscher, A. Pliss, T. Y. Ohulchanskyy and P. N. Prasad, *J. Am. Chem. Soc.*, 2016, **138**, 16192–16195.
- 50 W. Shao, C. K. Lim, Q. Li, M. T. Swihart and P. N. Prasad, *Nano Lett.*, 2018, **18**, 4922–4926.
- 51 W. Zou, C. Visser, J. A. Maduro, M. S. Pshenichnikov and J. C. Hummelen, *Nat. Photonics*, 2012, **6**, 560–564.
- 52 T. Liang, Q. Wang, Z. Li, P. Wang, J. Wu, M. Zuo and Z. Liu, *Adv. Funct. Mater.*, 2020, **30**, 1910765.
- 53 X. Wang, R. R. Valiev, T. Y. Ohulchanskyy, H. Ågren, C. Yang and G. Chen, *Chem. Soc. Rev.*, 2017, **46**, 4150–4167.
- 54 D. J. Garfield, N. J. Borys, S. M. Hamed, N. A. Torquato, C. A. Tajon, B. Tian, B. Shevitski, E. S. Barnard, Y. D. Suh, S. Aloni, J. B. Neaton, E. M. Chan, B. E. Cohen and P. J. Schuck, *Nat. Photonics*, 2018, **12**, 402–407.
- 55 S. Han, R. Deng, Q. Gu, L. Ni, U. Huynh, J. Zhang, Z. Yi, B. Zhao, H. Tamura, A. Pershin, H. Xu, Z. Huang, S. Ahmad, M. Abdi-Jalebi, A. Sadhanala, M. L. Tang, A. Bakulin, D. Beljonne, X. Liu and A. Rao, *Nature*, 2020, **587**, 594–599.

- 56 I. D. Hughes, M. Däne, A. Ernst, W. Hergert, M. Lüders, J. Poulter, J. B. Staunton, A. Svane, Z. Szotek and W. M. Temmerman, *Nature*, 2007, **446**, 650–653.
- 57 S. Amemori, Y. Sasaki, N. Yanai and N. Kimizuka, *J. Am. Chem. Soc.*, 2016, **138**, 8702–8705.
- 58 S. Wen, J. Zhou, P. J. Schuck, Y. D. Suh, T. W. Schmidt and D. Jin, *Nat. Photonics*, 2019, **13**, 828–838.
- 59 M. Green, E. Dunlop, J. Hohl-Ebinger, M. Yoshita, N. Kopidakis and X. Hao, *Prog. Photovoltaics*, 2021, **29**, 3–15.
- 60 J. C. Goldschmidt and S. Fischer, *Adv. Opt. Mater.*, 2015, **3**, 510–535.
- 61 K. W. Krämer, D. Biner, G. Frei, H. U. Güdel, M. P. Hehlen and S. R. Lüthi, *Chem. Mater.*, 2004, **16**, 1244–1251.
- 62 F. Wang, Y. Han, C. S. Lim, Y. Lu, J. Wang, J. Xu, H. Chen, C. Zhang, M. Hong and X. Liu, *Nature*, 2010, **463**, 1061–1065.
- 63 J. C. Boyer and F. C. J. M. van Veggel, *Nanoscale*, 2010, **2**, 1417–1419.
- 64 S. Fischer, J. C. Goldschmidt, P. Löper, G. H. Bauer, R. Brüggemann, K. Krämer, D. Biner, M. Hermle and S. W. Glunz, *J. Appl. Phys.*, 2010, **108**, 1–11.
- 65 B. M. van der Ende, L. Aarts and A. Meijerink, *Phys. Chem. Chem. Phys.*, 2009, **11**, 11081–11095.
- 66 H. Jia, Z. Liu, L. Liao, Y. Gu, C. Ding, J. Zhao, W. Zhang, X. Hu, X. Feng, Z. Chen, X. Liu and J. Qiu, *J. Phys. Chem. C*, 2018, **122**, 9606–9610.
- 67 J. Zhou, J. Deng, H. Zhu, X. Chen, Y. Teng, H. Jia, S. Xu and J. Qiu, *J. Mater. Chem. C*, 2013, **1**, 8023–8027.
- 68 R. Martín-Rodríguez, F. T. Rabouw, M. Trevisani, M. Bettinelli and A. Meijerink, *Adv. Opt. Mater.*, 2015, **3**, 558–567.
- 69 S. Fischer, B. Fröhlich, K. W. Krämer and J. C. Goldschmidt, *J. Phys. Chem. C*, 2014, **118**, 30106–30114.
- 70 Y. v. Orlovskii, T. T. Basiev, K. K. Pukhov, M. v. Polyachenkova, P. P. Fedorov, O. K. Alimov, E. I. Gorokhova, V. A. Demidenko, O. A. Khristich and R. M. Zakalyukin, *J. Lumin.*, 2007, **125**, 201–215.
- 71 R. Martín-Rodríguez, S. Fischer, A. Ivaturi, B. Froehlich, K. W. Krämer, J. C. Goldschmidt, B. S. Richards and A. Meijerink, *Chem. Mater.*, 2013, **25**, 1912–1921.
- 72 S. Fischer, R. Martín-Rodríguez, B. Fröhlich, K. W. Krämer, A. Meijerink and J. C. Goldschmidt, *J. Lumin.*, 2014, **153**, 281–287.
- 73 S. Fischer, R. D. Mehlenbacher, A. Lay, C. Siefe, A. P. Alivisatos and J. A. Dionne, *Nano Lett.*, 2019, **19**, 3878–3885.
- 74 F. Wang, J. Wang and X. Liu, *Angew. Chem., Int. Ed.*, 2010, **49**, 7456–7460.
- 75 S. F. Lim, W. S. Ryu and R. H. Austin, *Opt. Express*, 2010, **18**, 2309.
- 76 A. Skripka, A. Benayas, C. D. S. Brites, I. R. Martín, L. D. Carlos and F. Vetrone, *Nano Lett.*, 2020, **20**, 7648–7654.
- 77 F. T. Rabouw, P. T. Prins, P. Villanueva-Delgado, M. Castelijns, R. G. Geitenbeek and A. Meijerink, *ACS Nano*, 2018, **12**, 4812–4823.
- 78 M. Y. Hossan, A. Hor, Q. Luu, S. J. Smith, P. S. May and M. T. Berry, *J. Phys. Chem. C*, 2017, **121**, 16592–16606.
- 79 N. J. J. Johnson, S. He, S. Diao, E. M. Chan, H. Dai and A. Almutairi, *J. Am. Chem. Soc.*, 2017, **139**, 3275–3282.
- 80 S. Fischer, N. D. Bronstein, J. K. Swabeck, E. M. Chan and A. P. Alivisatos, *Nano Lett.*, 2016, **16**, 7241–7247.
- 81 N. J. J. Johnson, A. Korinek, C. Dong and F. C. J. M. van Veggel, *J. Am. Chem. Soc.*, 2012, **134**, 11068–11071.
- 82 F. Vetrone, R. Naccache, V. Mahalingam, C. G. Morgan and J. A. Capobianco, *Adv. Funct. Mater.*, 2009, **19**, 2924–2929.
- 83 C. Homann, L. Krukewitt, F. Frenzel, B. Grauel, C. Würth, U. Resch-Genger and M. Haase, *Angew. Chem., Int. Ed.*, 2018, **57**, 8765–8769.
- 84 Y. Hu, Q. Shao, Y. Dong and J. Jiang, *J. Phys. Chem. C*, 2019, **123**, 22674–22679.
- 85 S. Fischer, N. J. J. Johnson, J. Pichaandi, J. C. Goldschmidt and F. C. J. M. van Veggel, *J. Appl. Phys.*, 2015, **118**, 193105.
- 86 B. Zhou, B. Tang, C. Zhang, C. Qin, Z. Gu, Y. Ma, T. Zhai and J. Yao, *Nat. Commun.*, 2020, **11**, 1174.
- 87 O. Lehmann, K. Kömpe and M. Haase, *J. Am. Chem. Soc.*, 2004, **126**, 14935–14942.
- 88 K. Kömpe, O. Lehmann and M. Haase, *Chem. Mater.*, 2006, **18**, 4442–4446.
- 89 K. Kömpe, H. Borchert, J. Storz, A. Lobo, S. Adam, T. Möller and M. Haase, *Angew. Chem., Int. Ed.*, 2003, **42**, 5513–5516.
- 90 Y. Takeda, S. Mizuno, H. N. Luitel, K. Yamanaka and T. Tani, *Appl. Phys. Lett.*, 2016, **108**, 073102.
- 91 H. N. Luitel, S. Mizuno, T. Tani and Y. Takeda, *RSC Adv.*, 2016, **6**, 55499–55506.
- 92 Y. Wang, L. Tu, J. Zhao, Y. Sun, X. Kong and H. Zhang, *J. Phys. Chem. C*, 2009, **113**, 7164–7169.
- 93 D. O. Faulkner, S. Petrov, D. D. Perovic, N. P. Kherani and G. A. Ozin, *J. Mater. Chem.*, 2012, **22**, 24330–24334.
- 94 W. Shao, G. Chen, J. Damasco, X. Wang, A. Kachynski, T. Y. Ohulchanskyy, C. Yang, H. Ågren and P. N. Prasad, *Opt. Lett.*, 2014, **39**, 1386.
- 95 B. S. Richards, *Sol. Energy Mater. Sol. Cells*, 2006, **90**, 2329–2337.
- 96 B. S. Richards and A. Shalav, *IEEE Trans. Electron Devices*, 2007, **54**, 2679–2684.
- 97 A. Boccolini, R. Faoro, E. Favilla, S. Veronesi and M. Tonelli, *J. Appl. Phys.*, 2013, **114**, 064904.
- 98 A. Ivaturi, S. K. W. Macdougall, R. Martín-Rodríguez, M. Quintanilla, J. Marques-Hueso, K. W. Krämer, A. Meijerink and B. S. Richards, *J. Appl. Phys.*, 2013, **114**, 013505.
- 99 M. Rüdiger, S. Fischer, J. Frank, A. Ivaturi, B. S. Richards, K. W. Krämer, M. Hermle and J. C. Goldschmidt, *Sol. Energy Mater. Sol. Cells*, 2014, **128**, 57–68.
- 100 S. Fischer, E. Favilla, M. Tonelli and J. C. Goldschmidt, *Sol. Energy Mater. Sol. Cells*, 2015, **136**, 127–134.
- 101 C. M. S. Jones, N. Panov, A. Skripka, J. Gibbons, F. Hesse, J.-W. G. Bos, X. Wang, F. Vetrone, G. Chen, E. Hemmer and J. Marques-Hueso, *Opt. Express*, 2020, **28**, 22803.
- 102 G. E. Arnautakis, J. Marques-Hueso, A. Ivaturi, S. Fischer, J. C. Goldschmidt, K. W. Krämer and B. S. Richards, *Sol. Energy Mater. Sol. Cells*, 2015, **140**, 217–223.
- 103 C. L. M. Hofmann, S. Fischer, E. H. Eriksen, B. Bläsi, C. Reitz, D. Yazicioglu, I. A. Howard, B. S. Richards and J. C. Goldschmidt, *Nat. Commun.*, 2021, **12**, 104.

- 104 S. Fischer, A. Ivaturi, B. Frohlich, M. Rudiger, A. Richter, K. W. Kramer, B. S. Richards and J. C. Goldschmidt, *IEEE J. Photovoltaics*, 2014, **4**, 183–189.
- 105 A. C. Atre, A. García-Etxarri, H. Alaeian and J. A. Dionne, *J. Opt.*, 2012, **14**, 024008.
- 106 M. Wu, T. A. Lin, J. O. Tjepelt, V. Bulović and M. A. Baldo, *Nano Lett.*, 2021, **21**, 1011–1016.
- 107 C. L. M. Hofmann, B. Herter, S. Fischer, J. Gutmann and J. C. Goldschmidt, *Opt. Express*, 2016, **24**, 14895.
- 108 A. A. Ansari, M. K. Nazeeruddin and M. M. Tavakoli, *Coord. Chem. Rev.*, 2021, **436**, 1–23.
- 109 H. J. Snaith, *Adv. Funct. Mater.*, 2010, **20**, 13–19.
- 110 X. Xie, N. Gao, R. Deng, Q. Sun, Q. H. Xu and X. Liu, *J. Am. Chem. Soc.*, 2013, **135**, 12608–12611.
- 111 M. Liu, Y. Lu, Z. B. Xie and G. M. Chow, *Sol. Energy Mater. Sol. Cells*, 2011, **95**, 800–803.
- 112 G. B. Shan, H. Assaaoudi and G. P. Demopoulos, *ACS Appl. Mater. Interfaces*, 2011, **3**, 3239–3243.
- 113 C. Miao, T. Liu, Y. Zhu, Q. Dai, W. Xu, L. Xu, S. Xu, Y. Zhao and H. Song, *Opt. Lett.*, 2013, **38**, 3340–3343.
- 114 P. Ramasamy and J. Kim, *Chem. Commun.*, 2014, **50**, 879–881.
- 115 C. W. Kim, W. J. Shin, M. J. Choi, J. H. Lee, S. H. Nam, Y. D. Suh, Y. S. Kang and Y. S. Kang, *J. Mater. Chem. A*, 2016, **4**, 11908–11915.
- 116 K. Kakiage, Y. Aoyama, T. Yano, K. Oya, J. I. Fujisawa and M. Hanaya, *Chem. Commun.*, 2015, **51**, 15894–15897.
- 117 Z. Hosseini, N. Taghavinia and E. Wei-Guang Diao, *ChemPhysChem*, 2017, **18**, 3292–3308.
- 118 B. E. Hardin, E. T. Hoke, P. B. Armstrong, J. H. Yum, P. Comte, T. Torres, J. M. J. Fréchet, M. K. Nazeeruddin, M. Grätzel and M. D. McGehee, *Nat. Photonics*, 2009, **3**, 406–411.
- 119 J. M. Ji, H. Zhou, Y. K. Eom, C. H. Kim and H. K. Kim, *Adv. Energy Mater.*, 2020, **10**, 2000124.
- 120 W. R. Erwin, H. F. Zarick, E. M. Talbert and R. Bardhan, *Energy Environ. Sci.*, 2016, **9**, 1577–1601.
- 121 G. Y. Lee, K. Jung, H. S. Jang, J. Kyhm, I. K. Han, B. Park, H. Ju, S. J. Kwon and H. Ko, *Nanoscale*, 2016, **8**, 2071–2080.
- 122 G. B. Shan and G. P. Demopoulos, *Adv. Mater.*, 2010, **22**, 4373–4377.
- 123 S. Hore, C. Vetter, R. Kern, H. Smit and A. Hinsch, *Sol. Energy Mater. Sol. Cells*, 2006, **90**, 1176–1188.
- 124 C. Yuan, G. Chen, P. N. Prasad, T. Y. Ohulchanskyy, Z. Ning, H. Tian, L. Sun and H. Ågren, *J. Mater. Chem.*, 2012, **22**, 16709–16713.
- 125 L. Liang, Y. Liu, C. Bu, K. Guo, W. Sun, N. Huang, T. Peng, B. Sebo, M. Pan, W. Liu, S. Guo and X. Z. Zhao, *Adv. Mater.*, 2013, **25**, 2174–2180.
- 126 H. Guo, Z. Hu, L. Zhao, L. Wan, Y. Wu and S. Wang, *RSC Adv.*, 2017, **7**, 38506–38511.
- 127 N. C. Dyck and G. P. Demopoulos, *RSC Adv.*, 2014, **4**, 52694–52701.
- 128 Z. Zhou, J. Wang, F. Nan, C. Bu, Z. Yu, W. Liu, S. Guo, H. Hu and X. Z. Zhao, *Nanoscale*, 2014, **6**, 2052–2055.
- 129 P. Zhao, Y. Zhu, X. Yang, X. Jiang, J. Shen and C. Li, *J. Mater. Chem. A*, 2014, **2**, 16523–16530.
- 130 M. Luoshan, L. Bai, C. Bu, X. Liu, Y. Zhu, K. Guo, R. Jiang, M. Li and X. Zhao, *J. Power Sources*, 2016, **307**, 468–473.
- 131 N. Chander, A. F. Khan, V. K. Komarala, S. Chawla and V. Dutta, *Prog. Photovoltaics*, 2016, **24**, 692–703.
- 132 C. Yuan, G. Chen, L. Li, J. A. Damasco, Z. Ning, H. Xing, T. Zhang, L. Sun, H. Zeng, A. N. Cartwright, P. N. Prasad and H. Ågren, *ACS Appl. Mater. Interfaces*, 2014, **6**, 18018–18025.
- 133 T. Chen, Y. Shang, S. Hao, L. Tian, Y. Hou and C. Yang, *Electrochim. Acta*, 2018, **282**, 743–749.
- 134 P. Du, J. H. Lim, S. H. Kim and J. S. Yu, *Opt. Mater. Express*, 2016, **6**, 1896–1904.
- 135 P. Tadge, R. S. Yadav, P. K. Vishwakarma, S. B. Rai, T. M. Chen, S. Sapra and S. Ray, *J. Alloys Compd.*, 2020, **821**, 153230.
- 136 P. Du, J. H. Lim, J. W. Leem, S. M. Cha and J. S. Yu, *Nanoscale Res. Lett.*, 2015, **10**, 321–329.
- 137 J. Dutta, V. K. Rai, M. M. Durai and R. Thangavel, *IEEE J. Photovolt.*, 2019, **9**, 1040–1045.
- 138 R. Rajeswari, K. Susmitha, C. K. Jayasankar, M. Raghavender and L. Giribabu, *Sol. Energy*, 2017, **157**, 956–965.
- 139 R. Zhao, Q. Wu, D. Tang, W. Li, X. Zhang, M. Chen, R. Guo and G. Diao, *J. Alloys Compd.*, 2018, **769**, 92–95.
- 140 J. Yu, Y. Yang, R. Fan, P. Wang and Y. Dong, *Nanoscale*, 2016, **8**, 4173–4180.
- 141 M. Ambapuram, R. Ramireddy, G. Maddala, S. Godugunuru, P. V. S. Yerva and R. Mitty, *ACS Appl. Electron. Mater.*, 2020, **2**, 962–970.
- 142 Q. Li, J. Lin, J. Wu, Z. Lan, Y. Wang, F. Peng and M. Huang, *Electrochim. Acta*, 2011, **56**, 4980–4984.
- 143 G. Xie, Y. Wei, L. Fan and J. Wu, *J. Phys.: Conf. Ser.*, 2012, **339**, 012010.
- 144 J. Yu, Y. Yang, R. Fan, D. Liu, L. Wei, S. Chen, L. Li, B. Yang and W. Cao, *Inorg. Chem.*, 2014, **53**, 8045–8053.
- 145 L. Liang, Y. Yulin, Z. Mi, F. Ruiqing, Q. Lele, W. Xin, Z. Lingyun, Z. Xuesong and H. Jianglong, *J. Solid State Chem.*, 2013, **198**, 459–465.
- 146 J. H. Huang, P. Y. Hung, S. F. Hu and R. S. Liu, *J. Mater. Chem.*, 2010, **20**, 6505–6511.
- 147 J. Wu, J. Wang, J. Lin, Z. Lan, Q. Tang, M. Huang, Y. Huang, L. Fan, Q. Li and Z. Tang, *Adv. Energy Mater.*, 2012, **2**, 78–81.
- 148 J. Wang, J. Lin, J. Wu, M. Huang, Z. Lan, Y. Chen, S. Tang, L. Fan and Y. Huang, *Electrochim. Acta*, 2012, **70**, 131–135.
- 149 J. Yu, Y. Yang, R. Fan, H. Zhang, L. Li, L. Wei, Y. Shi, K. Pan and H. Fu, *J. Power Sources*, 2013, **243**, 436–443.
- 150 H. J. Snaith and L. Schmidt-Mende, *Adv. Mater.*, 2007, **19**, 3187–3200.
- 151 H. K. Ardakani, *Thin Solid Films*, 1994, **248**, 234–239.
- 152 B. Roose, S. Pathak and U. Steiner, *Chem. Soc. Rev.*, 2015, **44**, 8326–8349.
- 153 S. Mehra, S. Bishnoi, A. Jaiswal, M. Jagadeeswararao, A. K. Srivastava, S. N. Sharma and P. Vashishtha, *Energy Storage*, 2020, **2**, e120-28.
- 154 R. Asahi, Y. Taga and W. Mannstadt, *Phys. Rev. B: Condens. Matter Mater. Phys.*, 2000, **61**, 7459–7465.
- 155 S. Thomas, T. G. Deepak, G. S. Anjusree, T. A. Arun, S. V. Nair and A. S. Nair, *J. Mater. Chem. A*, 2014, **2**, 4474–4490.

- 156 G. Calogero, P. Calandra, A. Irrera, A. Sinopoli, I. Citro and G. di Marco, *Energy Environ. Sci.*, 2011, **4**, 1838–1844.
- 157 M. Ambapuram, G. Maddala, N. B. Simhachalam, S. Sripada, S. Kalvapalli, V. S. Yerva Pedda and R. Mitty, *Sol. Energy*, 2020, **207**, 1158–1164.
- 158 L. Li, Y. Yang, R. Fan, S. Chen, P. Wang, B. Yang and W. Cao, *ACS Appl. Mater. Interfaces*, 2014, **6**, 8223–8229.
- 159 B. O'Regan and M. Grätzel, *Nature*, 1991, **353**, 737–740.
- 160 T. Jiang, Z. Chen, X. Chen, T. Liu, X. Chen, W. E. I. Sha, H. Zhu and Y. Yang, *Sol. RRL*, 2020, **4**, 1900467.
- 161 D. Ramirez, K. Schutt, J. F. Montoya, S. Mesa, J. Lim, H. J. Snaith and F. Jaramillo, *J. Phys. Chem. C*, 2018, **122**, 21239–21247.
- 162 J. Jeong, M. Kim, J. Seo, H. Lu, P. Ahlawat, A. Mishra, Y. Yang, M. A. Hope, F. T. Eickemeyer, M. Kim, Y. J. Yoon, I. W. Choi, B. P. Darwich, S. J. Choi, Y. Jo, J. H. Lee, B. Walker, S. M. Zakeeruddin, L. Emsley, U. Rothlisberger, A. Hagfeldt, D. S. Kim, M. Grätzel and J. Y. Kim, *Nature*, 2021, **592**, 381–385.
- 163 H. S. Jung, G. S. Han, N. G. Park and M. J. Ko, *Joule*, 2019, **3**, 1850–1880.
- 164 X. Chen, W. Xu, H. Song, C. Chen, H. Xia, Y. Zhu, D. Zhou, S. Cui, Q. Dai and J. Zhang, *ACS Appl. Mater. Interfaces*, 2016, **8**, 9071–9079.
- 165 G. O. Kim and K. S. Ryu, *Bull. Korean Chem. Soc.*, 2012, **33**, 469–472.
- 166 D. Ma, Y. Shen, T. Su, J. Zhao, N. U. Rahman, Z. Xie, F. Shi, S. Zheng, Y. Zhang and Z. Chi, *Mater. Chem. Front.*, 2019, **3**, 2058–2065.
- 167 M. Schoenauer Sebag, Z. Hu, K. de Oliveira Lima, H. Xiang, P. Gredin, M. Mortier, L. Billot, L. Aigouy and Z. Chen, *ACS Appl. Energy Mater.*, 2018, **1**, 3537–3543.
- 168 F. L. Meng, J. J. Wu, E. F. Zhao, Y. Z. Zheng, M. L. Huang, L. M. Dai, X. Tao and J. F. Chen, *Nanoscale*, 2017, **9**, 18535–18545.
- 169 X. Lai, X. Li, X. Lv, Y. Z. Zheng, F. Meng and X. Tao, *J. Power Sources*, 2017, **372**, 125–133.
- 170 Z. Ning, X. Gong, R. Comin, G. Walters, F. Fan, O. Voznyy, E. Yassitepe, A. Buin, S. Hoogland and E. H. Sargent, *Nature*, 2015, **523**, 324–328.
- 171 L. Wang, I. King, P. Chen, M. Bates and R. R. Lunt, *APL Mater.*, 2020, **8**, 100904.
- 172 T. Leijtens, G. E. Eperon, S. Pathak, A. Abate, M. M. Lee and H. J. Snaith, *Nat. Commun.*, 2013, **4**, 2885.
- 173 L. Etgar, P. Gao, Z. Xue, Q. Peng, A. K. Chandiran, B. Liu, M. K. Nazeeruddin and M. Grätzel, *J. Am. Chem. Soc.*, 2012, **134**, 17396–17399.
- 174 L. Zhu, X. Shang, K. Lei, C. Wu, S. Zheng, C. Chen and H. Song, *Sol. RRL*, 2021, **5**, 2000605.
- 175 A. Filippetti, A. Mattoni, C. Caddeo, M. I. Saba and P. Delugas, *Phys. Chem. Chem. Phys.*, 2016, **18**, 15352–15362.
- 176 C. S. Ponseca, T. J. Savenije, M. Abdellah, K. Zheng, A. Yartsev, T. Pascher, T. Harlang, P. Chabera, T. Pullerits, A. Stepanov, J. P. Wolf and V. Sundström, *J. Am. Chem. Soc.*, 2014, **136**, 5189–5192.
- 177 G. Xing, B. Wu, S. Chen, J. Chua, N. Yantara, S. Mhaisalkar, N. Mathews and T. C. Sum, *Small*, 2015, **11**, 3606–3613.
- 178 X. X. Gao, Q. Q. Ge, D. J. Xue, J. Ding, J. Y. Ma, Y. X. Chen, B. Zhang, Y. Feng, L. J. Wan and J. S. Hu, *Nanoscale*, 2016, **8**, 16881–16885.
- 179 B. Roose, K. C. Gödel, S. Pathak, A. Sadhanala, J. P. C. Baena, B. D. Wilts, H. J. Snaith, U. Wiesner, M. Grätzel, U. Steiner and A. Abate, *Adv. Energy Mater.*, 2016, **6**, 1501868.
- 180 Z. Ren, J. Wu, N. Wang and X. Li, *J. Mater. Chem. A*, 2018, **6**, 15348–15358.
- 181 Z. Xu, J. Wu, T. Wu, Q. Bao, X. He, Z. Lan, J. Lin, M. Huang, Y. Huang and L. Fan, *Energy Technol.*, 2017, **5**, 1820–1826.
- 182 Z. Zhang, J. Qin, W. Shi, Y. Liu, Y. Zhang, Y. Liu, H. Gao and Y. Mao, *Nanoscale Res. Lett.*, 2018, **13**, 147.
- 183 M. Que, W. Que, X. Yin, P. Chen, Y. Yang, J. Hu, B. Yu and Y. Du, *Nanoscale*, 2016, **8**, 14432–14437.
- 184 M. He, X. Pang, X. Liu, B. Jiang, Y. He, H. Snaith and Z. Lin, *Angew. Chem., Int. Ed.*, 2016, **55**, 4280–4284.
- 185 H. Zhang, Y. Xiao, F. Qi, P. Liu, Y. Wang, F. Li, C. Wang, G. Fang and X. Zhao, *ACS Sustainable Chem. Eng.*, 2019, **7**, 8236–8244.
- 186 J. Roh, H. Yu and J. Jang, *ACS Appl. Mater. Interfaces*, 2016, **8**, 19847–19852.
- 187 Y. Li, L. Zhao, M. Xiao, Y. Huang, B. Dong, Z. Xu, L. Wan, W. Li and S. Wang, *Nanoscale*, 2018, **10**, 22003–22011.
- 188 Q. Guo, J. Wu, Y. Yang, X. Liu, J. Jia, J. Dong, Z. Lan, J. Lin, M. Huang, Y. Wei and Y. Huang, *J. Power Sources*, 2019, **426**, 178–187.
- 189 D. Zhou, D. Liu, J. Jin, X. Chen, W. Xu, Z. Yin, G. Pan, D. Li and H. Song, *J. Mater. Chem. A*, 2017, **5**, 16559–16567.
- 190 X. Wang, Z. Zhang, J. Qin, W. Shi, Y. Liu, H. Gao and Y. Mao, *Electrochim. Acta*, 2017, **245**, 839–845.
- 191 Y. Xiang, Z. Ma, J. Zhuang, H. Lu, C. Jia, J. Luo, H. Li and X. Cheng, *J. Phys. Chem. C*, 2017, **121**, 20150–20157.
- 192 P. Chen, Z. Wang, S. Wang, M. Lyu, M. Hao, M. Ghasemi, M. Xiao, J. H. Yun, Y. Bai and L. Wang, *Nano Energy*, 2020, **69**, 104392.
- 193 H. Li, B. Zheng, Y. Xue, S. Liu, C. Gao and X. Liu, *Sol. Energy Mater. Sol. Cells*, 2017, **168**, 85–90.
- 194 C. Chen, D. Liu, Y. Wu, W. Bi, X. Sun, X. Chen, W. Liu, L. Xu, H. Song and Q. Dai, *Nano Energy*, 2018, **53**, 849–862.
- 195 Q. Jiang, X. Zhang and J. You, *Small*, 2018, **14**, 1801154.
- 196 Z. Xu, S. H. Teo, L. Gao, Z. Guo, Y. Kamata, S. Hayase and T. Ma, *Org. Electron.*, 2019, **73**, 62–68.
- 197 H. J. Kim, U. Kim, H. M. Kim, T. H. Kim, H. S. Mun, B. G. Jeon, K. T. Hong, W. J. Lee, C. Ju, K. H. Kimy and K. Char, *Appl. Phys. Express*, 2012, **5**, 061102.
- 198 S. S. Shin, E. J. Yeom, W. S. Yang, S. Hur, M. G. Kim, J. Im, J. Seo, J. H. Noh and S. il Seok, *Science*, 2017, **356**, 167–171.
- 199 C. W. Myung, G. Lee and K. S. Kim, *J. Mater. Chem. A*, 2018, **6**, 23071–23077.
- 200 A. Corma, P. Atienzar, H. García and J. Y. Chane-Ching, *Nat. Mater.*, 2004, **3**, 394–397.
- 201 X. Wang, L. L. Deng, L. Y. Wang, S. M. Dai, Z. Xing, X. X. Zhan, X. Z. Lu, S. Y. Xie, R. bin Huang and L. S. Zheng, *J. Mater. Chem. A*, 2017, **5**, 1706–1712.
- 202 Z. Xing, S. H. Li, B. S. Wu, X. Wang, L. Y. Wang, T. Wang, H. R. Liu, M. L. Zhang, D. Q. Yun, L. L. Deng, S. Y. Xie,

- R. bin Huang and L. S. Zheng, *J. Power Sources*, 2018, **389**, 13–19.
- 203 T. Hu, S. Xiao, H. Yang, L. Chen and Y. Chen, *Chem. Commun.*, 2018, **54**, 471–474.
- 204 R. Meng, X. Feng, Y. Yang, X. Lv, J. Cao and Y. Tang, *ACS Appl. Mater. Interfaces*, 2019, **11**, 13273–13278.
- 205 G. Ren, W. Han, Y. Deng, W. Wu, Z. Li, J. Guo, H. Bao, C. Liu and W. Guo, *J. Mater. Chem. A*, 2021, **9**, 4589–4625.
- 206 F. Xu, Y. Sun, H. Gao, S. Jin, Z. Zhang, H. Zhang, G. Pan, M. Kang, X. Ma and Y. Mao, *ACS Appl. Mater. Interfaces*, 2021, **13**, 2674–2684.
- 207 Y. Ding, H. Qiao, T. Yang, N. Yin, P. Li, Y. Zhao and X. Zhang, *Opt. Mater.*, 2017, **73**, 617–622.
- 208 L. Xu, X. Chen, J. Jin, W. Liu, B. Dong, X. Bai, H. Song and P. Reiss, *Nano Energy*, 2019, **63**, 103860.
- 209 P. K. Kung, M. H. Li, P. Y. Lin, Y. H. Chiang, C. R. Chan, T. F. Guo and P. Chen, *Adv. Mater. Interfaces*, 2018, **5**, 1800882.
- 210 S. Teo, Z. Guo, Z. Xu, C. Zhang, Y. Kamata, S. Hayase and T. Ma, *ChemSusChem*, 2019, **12**, 518–526.
- 211 X. Chen, L. Xu, C. Chen, Y. Wu, W. Bi, Z. Song, X. Zhuang, S. Yang, S. Zhu and H. Song, *J. Power Sources*, 2019, **444**, 227267.
- 212 A. K. Jena, A. Kulkarni, Y. Sanehira, M. Ikegami and T. Miyasaka, *Chem. Mater.*, 2018, **30**, 6668–6674.
- 213 L. Wang, H. Zhou, J. Hu, B. Huang, M. Sun, B. Dong, G. Zheng, Y. Huang, Y. Chen, L. Li, Z. Xu, N. Li, Z. Liu, Q. Chen, L. D. Sun and C. H. Yan, *Science*, 2019, **363**, 265–270.
- 214 M. Wang, K. Deng, L. Meng and L. Li, *Small Methods*, 2020, **4**, 1900652.
- 215 B. J. Moon, S. J. Kim, S. Lee, A. Lee, H. Lee, D. S. Lee, T. W. Kim, S. K. Lee, S. Bae and S. H. Lee, *Adv. Mater.*, 2019, **31**, 1901716.
- 216 J. Liu, Q. Yao and Y. Li, *Appl. Phys. Lett.*, 2006, **88**, 86–89.
- 217 M. Zahedifar, Z. Chamanzadeh and S. M. Hosseinpour Mashkani, *J. Lumin.*, 2013, **135**, 66–73.
- 218 K. Sharma, V. Sharma and S. S. Sharma, *Nanoscale Res. Lett.*, 2018, **13**, 381.
- 219 C. Jiang and P. Song, *Nonlinear-Emission Photonic Glass Fiber and Waveguide Devices*, Cambridge University Press, 2019, pp. 145–176.
- 220 D. Chen, L. Lei, A. Yang, Z. Wang and Y. Wang, *Chem. Commun.*, 2012, **48**, 5898–5900.
- 221 J. A. Briggs, A. C. Atre and J. A. Dionne, *J. Appl. Phys.*, 2013, **113**, 124509.
- 222 W. Shao, G. Chen, T. Y. Ohulchanskyy, A. Kuzmin, J. A. Damasco, H. Qiu, C. Yang, H. Ågren and P. N. Prasad, *Adv. Opt. Mater.*, 2015, **3**, 575–582.
- 223 C. Yuan, G. Chen, L. Li, J. A. Damasco, Z. Ning, H. Xing, T. Zhang, L. Sun, H. Zeng, A. N. Cartwright, P. N. Prasad and H. Ågren, *ACS Appl. Mater. Interfaces*, 2014, **6**, 18018–18025.
- 224 S. Hao, Y. Shang, D. Li, H. Ågren, C. Yang and G. Chen, *Nanoscale*, 2017, **9**, 6711–6715.
- 225 H. Ning, L. Jing, Y. Hou, S. Kalytchuk, Y. Li, X. Huang and M. Gao, *ACS Appl. Mater. Interfaces*, 2020, **12**, 11934–11944.